



HAL
open science

Thermo-kinetic approach to the crystallization mechanism of thermochromic SmNiO₃ thin films: An in situ study in air-annealing

Zil Fernández-Gutiérrez, Stéphanie Bruyère, David Pilloud, Emile Haye, Ghouti Medjahdi, Silvère Barrat, Fabien Capon

► To cite this version:

Zil Fernández-Gutiérrez, Stéphanie Bruyère, David Pilloud, Emile Haye, Ghouti Medjahdi, et al.. Thermo-kinetic approach to the crystallization mechanism of thermochromic SmNiO₃ thin films: An in situ study in air-annealing. *Journal of Alloys and Compounds*, 2023, 960, pp.170799. 10.1016/j.jallcom.2023.170799 . hal-04121622

HAL Id: hal-04121622

<https://hal.univ-lorraine.fr/hal-04121622v1>

Submitted on 6 Nov 2023

HAL is a multi-disciplinary open access archive for the deposit and dissemination of scientific research documents, whether they are published or not. The documents may come from teaching and research institutions in France or abroad, or from public or private research centers.

L'archive ouverte pluridisciplinaire **HAL**, est destinée au dépôt et à la diffusion de documents scientifiques de niveau recherche, publiés ou non, émanant des établissements d'enseignement et de recherche français ou étrangers, des laboratoires publics ou privés.

Thermo-kinetic approach to the crystallization mechanism of thermochromic SmNiO_3 thin films: an *in situ* study in air-annealing

Zil Fernández-Gutiérrez^{a*}, Stéphanie Bruyère^a, David Pilloud^a, Emile Haye^b, Ghouti Medjahdi^a, Silvère Barrat^a, Fabien Capon^a

^aUniversité de Lorraine, CNRS, IJL, F-54000 Nancy, France

^bUniversité de Namur, LARN-NISM, B-5000 Namur, Belgium

*Email: zil.fernandez-gutierrez@univ-lorraine.fr

ABSTRACT

Rare-earth nickelates (RNiO_3) are an interesting oxide family because of their remarkable and reversible properties related to their structural changes. However, until recently, nickelates were difficult to synthesize without severe or sophisticated conditions. Consequently, a deep understanding of the nucleation and growth process for these versatile perovskites still lacks to date. Here, by correlation of the theory and the experimental data, is presented a clarification of the crystallization mechanism involved for $\text{SmNiO}_{3-\delta}$ thin films synthesized by a simple route that combines reactive magnetron sputtering and air-annealing. A thermo-kinetic approach to the amorphous-to-crystalline phase transformation is developed after following the evolution over time at 475, 500, and 525 °C through *in situ* high-temperature X-ray diffraction. Then, the kinetic parameters, the optimal temperature, and the necessary activation energy of transformation are determined from the Johnson-Mehl-Avrami-Kolmogorov (JMAK) model. Notably, the emergence of contrasting grains created on the free surfaces compared to the nanocrystallites formed from the bulk is revealed from the detailed study at 500 °C by Transmission electron microscopy. As classical nucleation theory outlines, such a growth difference is associated with heterogeneous and homogeneous processes. Furthermore, the

progression with the annealing time of the crucial stabilization of the Ni^{3+} and the electronic structure is analyzed by Electron energy-loss spectroscopy and X-ray photoelectron spectroscopy. Finally, the optical properties measurements demonstrate a metal-insulator transition (MIT) at 125 °C, a thermochromic performance of 32%, and mainly, the crystallization significance to achieve functional nickelates thin films, which pave the way as promising candidates for solar thermal applications.

Keywords: Perovskite thin film; Crystallization mechanism; JMAK model; Classical nucleation theory; Thermochromic material

1. INTRODUCTION

Rare-earth nickelates (RNiO_3) are a fascinating perovskite family that exhibits an extensive landscape of applications in optoelectronic [1–7], resistance switching [8–14], magnetism [15–20], supercapacitor [21–23], and sensing [24,25], to cite a few. Furthermore, one of their most appealing phenomena is the metal-insulator transition (MIT), which allows a reversible change in the physical properties at a critical temperature (T_{MI}) [26–28]. Therefore, nickelates are categorized among the negative charge-transfer insulators, in which an electron-lattice coupling has an essential role [29–31]. Indeed, by varying the rare-earth (R) ionic radius, the distortion of the oxygen octahedra is modified, and consequently, the Ni-O bond and the T_{MI} . Then, it allows the MIT adjustability in a wide temperature range with values around -140, -70, 127, and 324 °C, for $R = \text{Pr, Nd, Sm, and Lu}$, respectively [20,26,31–33].

Despite their promising functionalities, their use and study are still limited due to the complexity of their elaboration. Even if the RNiO_3 oxides have been synthesized since 1971 [34], conventional procedures cannot be employed given their high metastability (for $R \neq \text{La}$) and the difficulty of stabilizing the Ni^{3+} ion and the corresponding orthorhombic structure [14].

Hence, in bulk or thin films, several works reported the need to crystallize these perovskites under extreme annealing conditions at high oxygen pressures and temperatures [26,35–39]. Additionally, epitaxial films constitute the predominant alternative for producing high-quality samples [40–47]. However, it requires specific and expensive substrates and is limited to small surfaces. Besides that, it is only feasible through techniques such as molecular beam epitaxy (MBE) or pulsed laser deposition (PLD), which demand careful handling for an outstanding result [33].

Much research effort has been spent on achieving nickelates without these peculiar requirements, which unlike other perovskite systems (e.g., $R\text{FeO}_3$, $R\text{CoO}_3$, $R\text{MnO}_3$), present a positive free energy of formation ΔG [35,39]. This latter, together with the problematic oxidation of Ni^{3+} since Ni^{2+} is the most stable oxidation state, represents the greatest challenge in stabilizing this material family. Nevertheless, our previous work demonstrated the feasibility of obtaining thermochromic $\text{SmNiO}_{3-\delta}$ thin films by a soft-synthesis route combining reactive magnetron sputtering and air-annealing [48]. Even if it constitutes a significant step forward for producing nickelates in sizeable samples and contemplates their use on an industrial scale, it is intriguing to explore in depth the achievement of this functional oxide in such a simple way. Mainly, a higher distortion of the SmNiO_3 structure adds a degree of difficulty due to the rare-earth size, which disfavors its crystallization [33,49–51].

A deep understanding of the nucleation and growth mechanisms involved in the crystallization process for nickelates is lacking in the literature due to the adversity of synthesizing them without severe and sophisticated conditions. Therefore, the present work provides for the first time a thermo-kinetic approach to the amorphous-to-crystalline phase transformation of SmNiO_3 thin films. For that purpose, a kinetic study of the crystallization evolution over time at three different temperatures is conducted through *in situ* high-temperature X-ray diffraction (HTXRD) measurements in air. It enables us to determine the kinetic parameters and the

activation energy for the crystallization of this compound from the model of Johnson-Mehl-Avrami-Kolmogorov (JMAK). Furthermore, a detailed structural analysis of the progression at various annealing times is performed by transmission electron microscopy (TEM). The latter revealed a combination of heterogeneous and homogeneous processes due to the grain's emergence, which is correlated with the classical nucleation theory [52]. Moreover, the electronic configuration was followed through EELS and XPS analyses, evidencing the gradual stabilization of the Ni^{3+} ion with the annealing time and the crystallization increase. Finally, the optical properties were measured by FTIR spectroscopy to corroborate the metal-insulator transition (MIT) and the thermochromic performance of the SmNiO_3 thin film. The crystallization mechanisms and their corresponding evolution are crucial aspects for the synthesis and properties of nickelates. Therefore, using an easier methodology, this work serves as a platform for future investigations and developments of RNiO_3 perovskite thin films.

2. EXPERIMENTAL DETAILS

Thin films synthesis: Amorphous Sm-Ni-O thin films (160 nm thick) were deposited on undoped (100)-silicon substrates by reactive magnetron sputtering. In an Ar:O₂ atmosphere (51:17 sccm) at 0.5 Pa, the Ni and Sm metallic targets (99.9% of purity, 50.8 mm in diameter and thicknesses of 1.5 mm (Ni) and 3 mm (Sm)) were sputtered by a DC generator (0.08 A) and a pulsed-DC power supply (0.48 A, 50 kHz, 4 μ s), respectively. The target-substrate distance was 10 cm, while the substrate holder rotated at 6 rpm to guarantee the samples homogeneity. No intentional heating was applied during deposition, as described in [48]. Then, to crystallize the films, the samples were annealed in air at 500 °C for 5 and 120 min in a rapid thermal annealing (RTA) furnace (AS-One 100). A heating ramp of 25 °C/s was applied to reach the desired temperature.

Thin films characterization: X-ray diffractograms (XRD) (between $20^\circ < 2\theta < 65^\circ$) were recorded on a Bruker D8 Advance diffractometer operating in Bragg Brentano configuration with $\text{CuK}\alpha_1$ radiation ($\lambda = 1.5406 \text{ \AA}$). For the *in situ* high-temperature X-ray diffraction measurements (HTXRD, between $22^\circ < 2\theta < 36^\circ$), the samples were annealed in air at 475, 500 and 525 °C in an oven-chamber Anton Paar HTK 1200, which is installed inside an Xpert Pro MPD diffractometer with the same configuration. The lattice parameters were determined by the DIFFRAC.EVA Bruker's suite. Transmission electron microscopy (TEM) was carried out with a JEOL ARM 200-Cold FEG. Cross-sectional TEM samples of films were elaborated employing a focused ion beam (FIB)-SEM dual beam system (FEI Helios Nanolab 600i). Electron energy loss spectroscopy (EELS) measurements were conducted in scanning electron transmission microscopy mode (STEM). The spectrometer (a GATAN GIF Quantum ER) was set to an energy dispersion of 0.05 eV/channel and a zero-loss peak with a FWHM lower than 0.6 eV. Digital Micrograph[®] was used for TEM and EELS image processing and data analysis. X-ray photoelectron spectroscopy (XPS) analysis was performed on a Thermo Escalab 250Xi spectrometer, working with Al K α (1486.68 eV), with a spot size of 250x250 μm . The core level spectra of O 1s, Ni 2p, and Sm 3d and valence band spectra were acquired with a pass energy of 20 eV, with scan numbers between 20 to 64. Prior to analysis, the surface was cleaned by Argon cluster (Ar₅₀₀₊, 120 s) to prevent contamination. A flood gun has been used for the study, and no further energy shift has been applied to the spectra. Considering a Shirley background, the spectra were fitted with Thermo Advantage[™] software.

Optical measurements: A Jasco FT/IR-6600 spectrometer measured the transmittance evolution in a wavelength range of 2.5-25 μm . With a Linkam FTIR600, the samples were heated from 30 to 270 °C each 30 °C. The background corresponded to the signal from the silicon substrate fixed on the Linkam FTIR600, which was located in the IR beam trajectory.

3. RESULTS AND DISCUSSIONS

3.1. *In situ* study of phase transformation kinetics

The amorphous-to-crystalline phase transformation of *samarium nickelate* ($\text{SmNiO}_{3-\delta}$) thin films can be first followed through *in situ* high-temperature X-ray diffraction (HTXRD) measurements. The crystallization evolution with time at 500 °C in the range of $22^\circ < 2\theta < 36^\circ$ is depicted in **Figure 1(a)**. The as-deposited sample is amorphous, while at 10 min, the first diffraction peak of the perovskite phase appears at the 2θ angle value of 33.6° . Then, the latter's evolution continues at 20 min, as well as the appearance of a second peak at 23.7° , related to the (002) plane. Thus successively, the crystallization of the material progresses until a third peak can be observed at 26.4° corresponding to the (111) diffraction plane.

This type of measurement allows to determine the parameters involved in the crystallization kinetics of the material through the classic theory of Johnson-Mehl-Avrami-Kolmogorov (JMAK) [53–57]. Due to its simplicity and effectiveness, this model can be used to study phase transformation kinetics in bulk and thin films. The JMAK model is based on the geometrical evolution of an extended volume of transformations that occurs *via* nucleation and growth mechanisms [58]. The most widely used format of the JMAK equation is:

$$f_V = 1 - \exp(-kt^n) \quad (1)$$

where, f_V is the transformed volume fraction, k is the reaction rate constant, t is time, and n is the Avrami exponent. Moreover, rearranging **Eq. (1)**, it is found the expression commonly used to construct the Avrami plot, which is pretty informative and easily elucidates the kinetic parameters' comparison:

$$\ln(-\ln(1 - f_V)) = \ln(k) + n \ln(t) \quad (2)$$

Hence, to put the JMAK model into practice, the amorphous-to-crystalline phase transformation of *samarium nickelate* thin films was recorded every 10 min for 6 h at 425, 500, and 525 °C. The selection of temperatures was given by the crystallization temperature already reported in our previous work (500 °C) [48]. Regarding that in **Figure 1(a)**, there is no evolution of the peaks between 120 min and 360 min; then, it can be considered that the maximum crystallization has been reached for the temperature of 500 °C after 6 h of annealing ($f_V = 1$). Another piece of evidence is the disappearance of the characteristic amorphous hump between 28-32°.

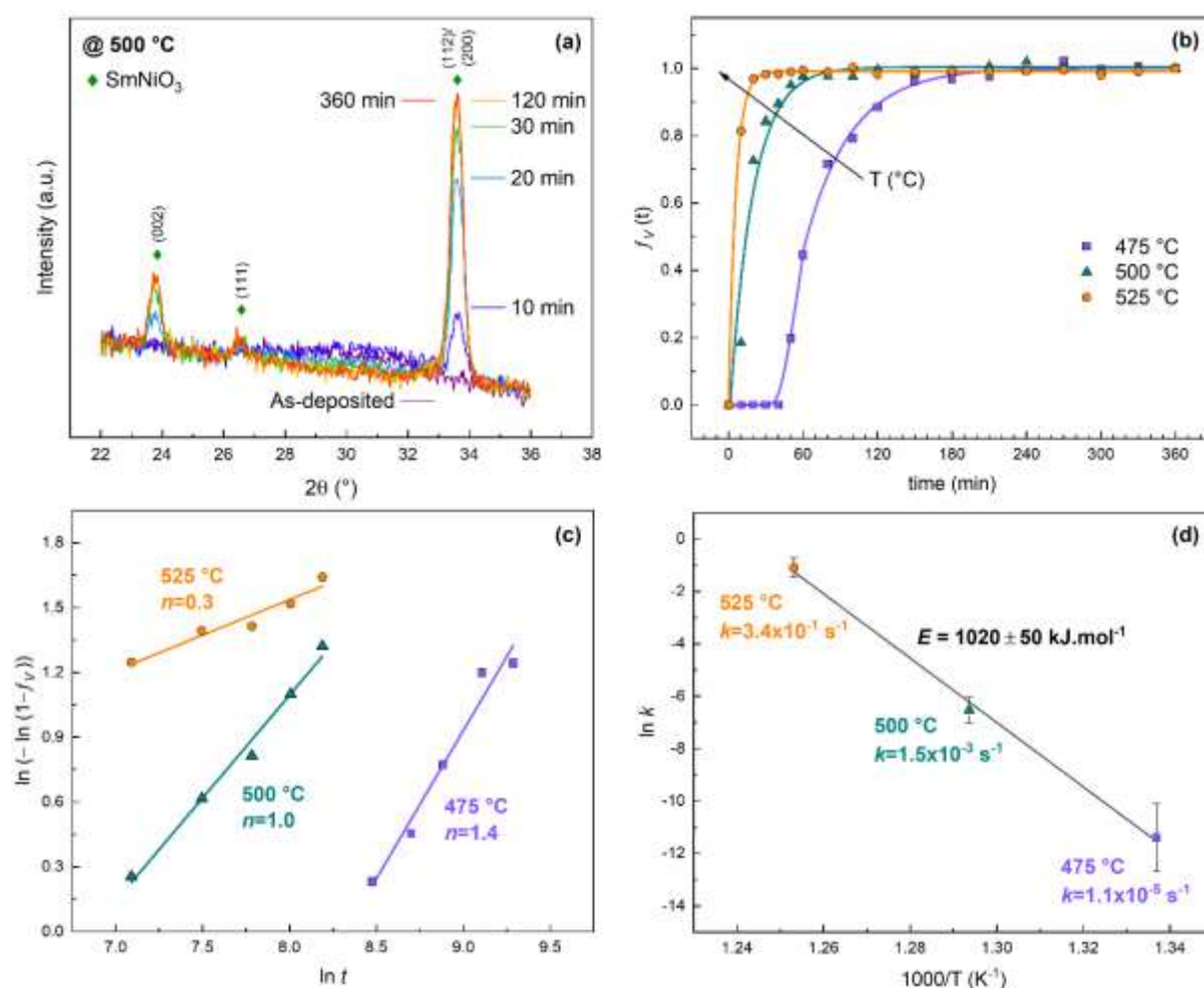


Figure 1. Crystallization evolution by *in situ* high temperature X-ray diffraction (HTXRD) measurements at 475, 500 and 525 °C. (a) XRD patterns at 500 °C for different times in the range of $22^\circ < 2\theta < 36^\circ$. (b) The transformed volume fraction progress with time. (c) The Avrami plot of the kinetic model fitting described by **Eq. (2)**. (d) Determination of the activation energy of the reaction by the fitting described by **Eq. (4)**.

Then, taking this case as a reference, the evolution of the transformed volume fraction (f_V) with time was determined by calculating the area under the most intense diffraction peak (112) at 33.6° . The crystallization progression of each isothermal reaction is displayed in **Figure 1(b)**. As can be observed, the increase in temperature accelerates the crystallization process. Indeed, at 475°C , the amorphous-to-crystalline transformation starts from 50 min (incubation time). On the contrary, for the other two temperatures, even though both progressions have already begun at 10 min, the transformed fraction is around 0.2 and 0.8 at 500°C and 525°C , respectively, without any visible incubation time.

The effect of temperature can be more easily seen on the Avrami plot in **Figure 1(c)**. The fitted lines by **Eq. (2)** reveal the increase in crystallization kinetics at higher temperatures and give access to the parameters n and k summarized in **Table 1**. A rise of two orders of magnitude in the reaction rate constant (k) is generated with every 25°C change in temperature, going from 1.13×10^{-5} to $3.37 \times 10^{-1} \text{ s}^{-1}$ at 475°C and 525°C , respectively.

Table 1. Parameters involved in the crystallization of $\text{SmNiO}_{3.8}$ thin films: the Avrami exponent (n), the reaction rate constant (k), the activation energy (E).

T ($^\circ\text{C}$)	n	$\ln k$	k (s^{-1})	E
475	1.4	-11.4	1.13×10^{-5}	1020 ± 50
500	1.0	-6.5	1.47×10^{-3}	kJ mol^{-1}
525	0.3	-1.1	3.37×10^{-1}	

It is important to note that some authors have emphasized that in thin films, the assumptions of the JMAK equations are not upheld. As growing particles impinge upon free surfaces, the infinite size assumption is not entirely accurate. In addition, heterogeneous nucleation from an interface is favored in many systems, partially infringing the random homogeneous nucleation (bulk). It may be the cause of certain anomalous Avrami exponents (n) and nonlinear Avrami plots [58,59]. However, a consensus or a more efficient way than through experimental data

has not been found. Here, to avoid irregularities in the values of n , the Avrami plot (**Figure 1(c)**) was constructed over the course of the transformation (i.e., with the points obtained from the nucleation beginning until the first value reached $f_V = 0.98$). Also, samples of the same thickness were used since the latter's effect on the Avrami exponent has been highlighted [59].

In this sense, a necessary remark is about the Avrami exponent (n) of 0.3 for the isothermal reaction at 525 °C. This parameter is independent of temperature and contains information about dimensional growth. Nevertheless, phase transitions with low values of n are related to crystal defects such as dislocations and vacancies [60,61]. Indeed, the comparison in **Figure 2** of the last X-ray diffractograms (after 6 h for each temperature) shows that although the crystallization at 525 °C is the fastest, it does not mean it is the best. Besides that, the transformation at 475 °C is unfinished. The diffraction peak (112) is less intense at this temperature than at 500 °C. Nevertheless, unlike the case at 525 °C, at least it follows the same behavior as the reaction at 500 °C. Most of the peaks are present and the slope in **Figure 1(c)** is also similar.

Then, some assumptions can be made from this result. For the first one, it is crucial to keep in mind that the crystallization of amorphous materials occurs when thermal energy, greater than the activation energy, is supplied for a sufficient time. Therefore, for transformation kinetics that are too fast, it is possible that the time necessary to obtain an acceptable nucleation rate allowing the subsequent grain growth stage may not be reached, favoring the presence of defects or oxygen vacancies instead. Second, 525 °C is perhaps the beginning of the crystallization of another oxide. Actually, in our previous work [48], it was shown that at 600 °C the favored phase was the Sm_2O_3 oxide and not the SmNiO_3 perovskite. Whether due to a loss of oxygen, the creation of defects, or an oxide phase change, 525 °C is not the ideal crystallization temperature for this nickelate. From **Figure 2**, it is clear that the crystallization

after 6 h at 475 °C and 525 °C only represents a partial percentage of the crystallization evidenced at 500°C.

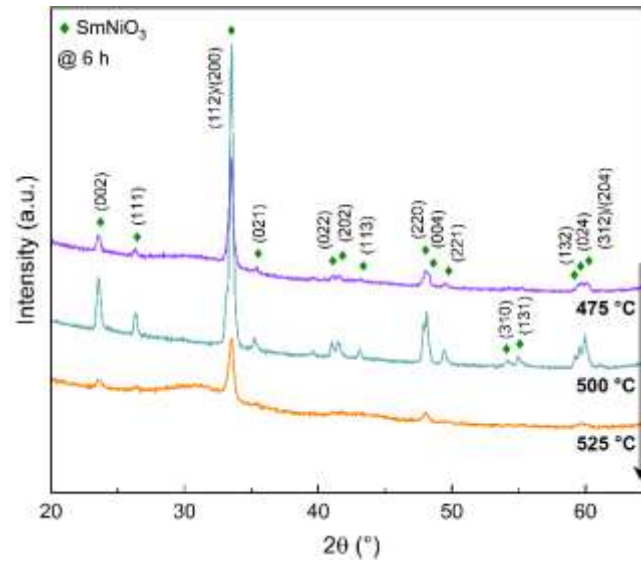


Figure 2. Comparison of the X-ray diffractograms after the *in situ* analysis for 6 h at 475 °C, 500 °C and 525 °C. The (hkl) labels correspond to the SmNiO₃ diffraction pattern (PDF n° 80-1948)

Finally, another meaningful information that can be extracted from these results is the calculation of the activation energy of the amorphous-to-crystalline transformation of this type of perovskites. From the Arrhenius equation, the reaction rate constant and temperature show the following relationships:

$$k = A \cdot \exp(-E/RT) \quad (3)$$

$$\ln k = \ln A - E/RT \quad (4)$$

where, A is the pre-exponential factor, E is the activation energy for the reaction, R is the universal gas constant, and T is the isothermal temperature. In **Figure 1(d)**, the linear regression fitting represents the slope in **Eq. (4)** and yields the calculation of the activation energy of SmNiO_{3-δ} phase transformation, equal to 1020 ± 50 kJ/mol.

To the best of our knowledge, no activation energy (E) for nucleation value has been reported for SmNiO_3 thin films, due to the difficulty of synthesizing it without high oxygen pressures. Here, air-annealing allowed to obtain an estimate value of E for the nucleation of this material, corroborating the challenge of crystallizing this nickelate. In fact, the comparison with other perovskites confirms that this energy value is quite high. For PZT thin films, the initial nucleation from the pure amorphous phase generally has much higher activation energy (441 kJ/mol) than the crystal growth from nucleates (112 kJ/mol) [62]. Another case is the reported values for orthoferrite perovskites ($R\text{FeO}_3$) which are influenced by the ionic radius of the rare-earth (R). The energy needed for LaFeO_3 crystallization (302 kJ/mol) was less than half that for SmFeO_3 (669 kJ/mol) [63]. The last one is a clear example since the crystallization conditions of orthoferrites are less severe than for nickelates.

Therefore, it can be considered that the value obtained in this work is congruent to the order of magnitude as other perovskites. Activation energies of 1443 kJ/mol have been reported for other complex oxides in thin layers [64], which would place our result in the same range. In especial, it must be noted that here, it began from an absolutely amorphous layer, which is also tricky to crystallize due to the significant distortion in SmNiO_3 perovskites.

3.2. Microscopic analysis of the crystalline structural evolution

As the XRD patterns showed more intense diffraction peaks for $\text{SmNiO}_{3-\delta}$ thin films annealed at 500 °C, it was decided to explore in-depth the actual state of the amorphous-to-crystalline phase transformation with time. Hence, it was chosen to study the progression from an as-deposited sample to another annealed for 120 min to ensure that $f_V = 1$ at 500 °C (see **Figure 1(b)**). As an intermediate point, it was intriguing to analyze a new duration and especially what happens at 5 min.

First, to verify the evolution of all diffraction peaks with time in the entire range of $20^\circ < 2\theta < 65^\circ$, the structural characterization by XRD was performed and is displayed in **Figure 3**. As shown, the as-deposited sample is fully amorphous, and after 5 minutes of annealing, some peaks appear around 33.6° , 48.2° , and 59.9° . Nevertheless, as expected for the 120 min case, all the peaks of the perovskite phase are identified (PDF 80-1948). Then, the orthorhombic unit cell parameters calculated from the annealed sample for 120 min are compared with the values obtained in [27] (**Table 2**).

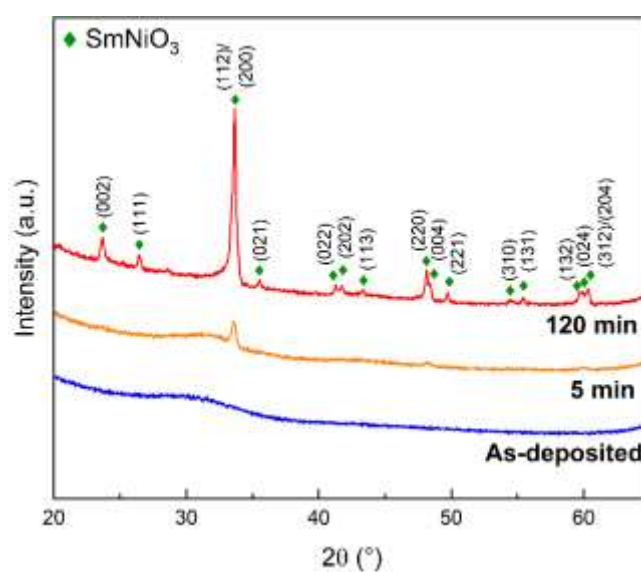


Figure 3. X-ray diffractograms of the as-deposited and amorphous Sm-Ni-O layer and the resulting crystallized $\text{SmNiO}_{3.8}$ thin films after air-annealing at 500°C for 5 min and 120 min, respectively. The (hkl) labels correspond to the SmNiO_3 diffraction pattern (PDF n° 80-1948).

Table 2. Lattice parameters of the orthorhombic SmNiO_3 calculated in this work as compared with the data of previous works on samarium nickelates.

	a (Å)	b (Å)	c (Å)	V (Å ³)
Reference [27]	5.33	5.43	7.56	218.8
This work	5.30	5.37	7.52	214.0
Deviation (%)	-0.6	-1.1	-0.5	-2.2

A very low deviation is observed, corresponding to a smaller unit cell that favors the stabilization of the Ni^{3+} oxidation state. Indeed, it has been demonstrated that for larger lattice

parameters there is a strain relaxation, which leads to the transformation from Ni^{3+} into Ni^{2+} (with a bigger ionic radius) and gives rise to the formation of oxygen vacancies [33,39,65]. This is a fruitful result since it may explain the crystallization of SmNiO_3 thin films on silicon substrates by the synthesis process described in this work. Meaning that air-annealing not only reaches the activation energy necessary for phase transformation but also guarantees the minimum strain relaxation to crystallize this challenging material.

A detailed cross-sectional study of the crystallization evolution by transmission electron microscopy (TEM) for the different annealing duration was carried out. The perovskite phase transformation is exposed in **Figure 4**, elucidating the possible mechanisms involved. Indeed, a clear change between the amorphous state (**Figures 4(a-b)**) and the air-annealed samples can be observed. The early stage of crystallization at 5 min displays the film formation in **Figure 4(c)** where it can be identified the preferential sites to nucleate and growth: the substrate-film interface, the bulk film, and the top-film surface. As can be seen, three-grain growth started from the film's top and the substrate's interface. But also, spherical nanocrystallites produced within the bulk of the amorphous phase can also be discerned. The SmNiO_3 phase was confirmed in both cases through selected area electron diffraction (SAED). **Figures 4(d)** and **4(e)** depict the SAED pattern, which resulted in polycrystalline and single-crystalline structures, respectively.

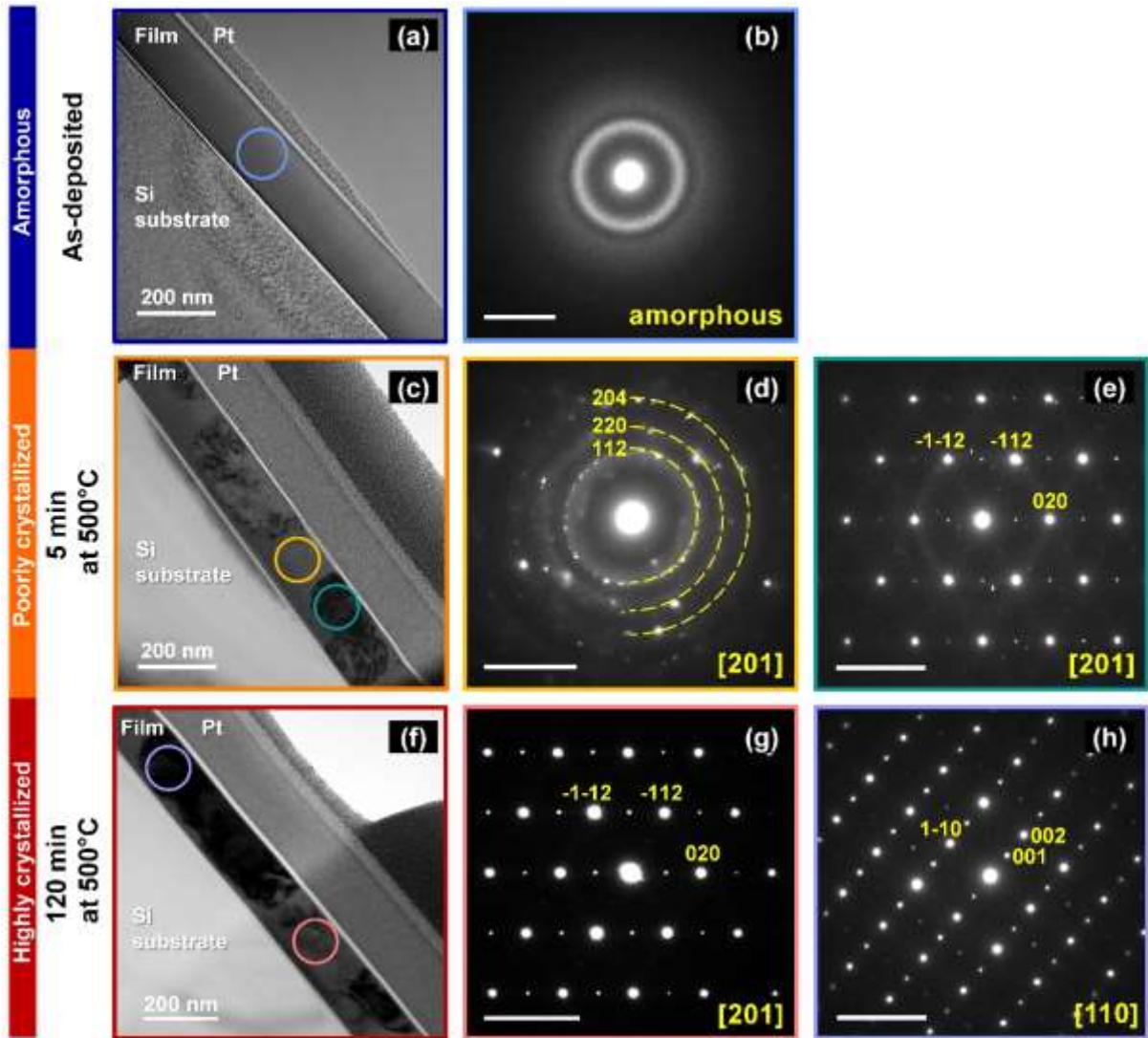


Figure 4. Cross-sectional study by transmission electron microscopy (TEM) of the crystallization evolution from the amorphous Sm-Ni-O layer to the crystallized air-annealed SmNiO_{3.8} films. First column: Bright-field images of the as-deposited and the air-annealed films. The contrast difference is the result of oriented grains in a diffraction position. Second and third column: SAED patterns corresponding to the circles inside the first column images revealing the amorphous, polycrystalline and monocrystalline states. SAED scale bar: 5 nm⁻¹.

On the other hand, the air-annealed layer for 120 min is presented in **Figure 4(f)**. The bright-field image, in which the difference in contrast exposes the diverse crystallographic orientations, uncovers the enormous grains throughout the thickness of the SmNiO_{3.8} film. Also, the SAED patterns in **Figures 4(g)** and **4(h)** of the two highlighted grains confirm that they are monocrystalline. Besides that, in the nearby areas, the grain boundaries reveal other

large grains. These results agree with the *in situ* HTXRD measurements and confirm the polycrystalline film's complete phase transformation. By extension, we can assume that this stage is the result of the formation of crystallites that grew at the expense of the amorphous matrix and the eventual coalescence process until reaching the grain impingement.

Finally, the crystallization grade of the sample is shown in **Figure 5(a)** through a high-angle annular dark-field scanning transmission electron microscopy (HAADF-STEM) image. The latter brings out the atomic arrangement in a highly ordered structure of the SmNiO₃ phase of the grain highlighted with the purple circle in **Figure 4(f)**. It is noteworthy that such a level of crystallization and order in SmNiO₃ thin films has only been evidenced in epitaxial superlattice (of no more than 50 nm) grown on LaAlO₃ substrates [41,43]. Only Napierala *et al.* [38] have shown a similar atomic organization on a silicon substrate for Nd_{0.3}Sm_{0.7}NiO₃ films, but in their case, the layers were annealed under high oxygen pressures.

Here, the [110] orientation of the diffracted grain reveals the small zig-zag displacement of the samarium atoms (pink line in **Figures 5(a-b)**). This atomic organization is also visible and analogous both to the simulated HAADF image and to the unit cell for the same zone axis in **Figures 5(b)** and **5(c)**, respectively. It is essential to point out that the intensity in a HAADF image is atomic number (Z) dependent due to the high collection angle. The contrast is approximately proportional to the square of the atomic number. Then, only the Sm ($Z = 62$) atoms are observable because of the difference in Z with O (8) and Ni (28).

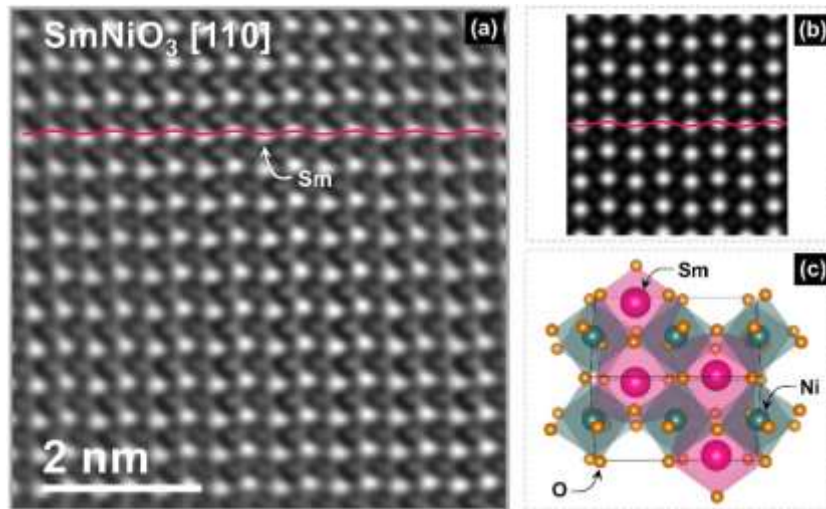


Figure 5. The atomic arrangement of the $\text{SmNiO}_{3-\delta}$ thin film along the [110] zone axis. (a) Experimental HAADF-HRSTEM image of the grain highlighted with the purple circle in **Figure 4(f)**. (b) Simulated HAADF image using the JEMS software [66]. (c) Samarium nickelate (SmNiO_3) unit cell. Note the zig-zag displacement (indicated by the pink line) of the samarium atoms for a same row in both the experimental and theoretical images.

3.3. Crystallization mechanisms: correlation between theory and experimental results

Based on the obtained results, some hypotheses can be made even if the dividing line between the end of nucleation and the beginning of growth is not sharply defined. Mainly because both processes frequently happen simultaneously in different parts of the same system [67]. The remarkable difference at 5 min, between the size of the grains created on the free surfaces compared to the nanocrystallites formed from the bulk, leads us to the first assumption: the presence of a combination of heterogeneous and homogeneous processes.

For the large grains, because of the effective reduction in surface energy, cap nuclei appear first (**Figure 6(a)**), and the formation rate is greater relative to that obtained by homogeneous nucleation (**Figure 6(b)**). Indeed, less energy is expended in creating the cap heterogeneously than in creating spherical nuclei homogeneously. Thus, since there are zones that crystallize from the bulk in a homogeneous way, even if large grains are seen, the annealing time of 5 minutes is not enough to obtain a complete crystallization, as illustrated in **Figure 6(c)**.

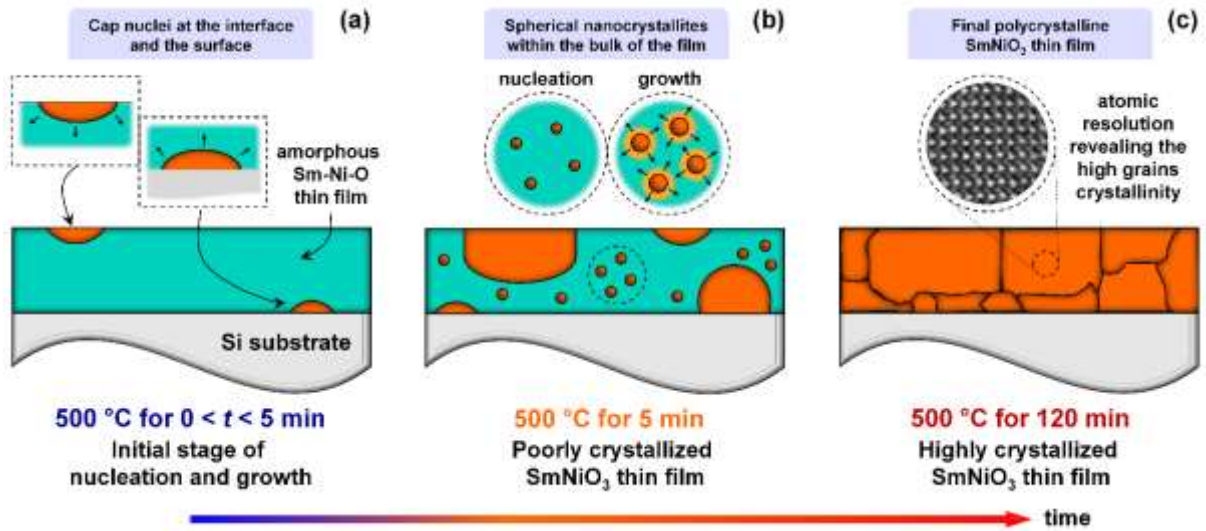


Figure 6. Schematic of the nucleation and growth process over time at 500 °C in $\text{SmNiO}_{3.6}$ thin films *via* air-annealing in the RTA furnace.

This crystallization process can be explained by classical nucleation theory. If it is considered that this kind of perovskite nucleates as spheroidal nuclei inside the amorphous phase, then their formation is governed by homogeneous nucleation. In this context, the stability of a perovskite nucleus (p) (with a radius r) from the surrounding amorphous phase (a) is described by the variation of the characteristic function ΔG . It gives the total free energy change between these two different states and decreases when the transformation is spontaneous:

$$\Delta G = -\frac{4}{3}\pi r^3 \left[\frac{\Delta_a^p G_m}{V_m^p} - \Delta_a^p G_{ES} \right] + 4\pi r^2 \gamma \quad (5)$$

$$\Delta_a^p G_m = G_m^p - G_m^a \quad (6)$$

and, V_m^p is the perovskite molar volume, and γ and $\Delta_a^p G_m$ are the surface tension and the molar Gibbs free energy between the perovskite (p) and the amorphous (a) phases, respectively. More precisely, $\Delta_a^p G_m$ is described by **Eq. (6)** and corresponds to the crystallization driving force [68], which is a negative value as soon as the amorphous phase is reached during deposition. Also, the term $\Delta_a^p G_{ES}$ represents the Gibbs free energy linked to the elastic strain change per unit

volume of the formed crystalline phase. According to V. Raghavan and Morris Cohen [69], it can be evaluated through:

$$\Delta_a^p G_{ES} = \frac{2}{3} \mu \left(\frac{\Delta V}{V} \right)^2 \quad (7)$$

where, μ is the shear modulus of the amorphous phase (taken to be elastically isotropic), and $\Delta V/V$ is the fractional volume change accompanying the transformation. The $\Delta_a^p G_{ES}$ factor is always positive, opposing the crystallization driving force in **Eq. (5)**, and therefore hindering the nucleation of the perovskite phase. Schematic diagrams in **Figures 7(a)** and **7(b)** illustrate the component's contribution in **Eq. (5)**, and the elastic strain influence ($\Delta_a^p G_{ES}$) in the characteristic function evolution (in terms of critical radius r^* and barrier to overcome ΔG^*), respectively.

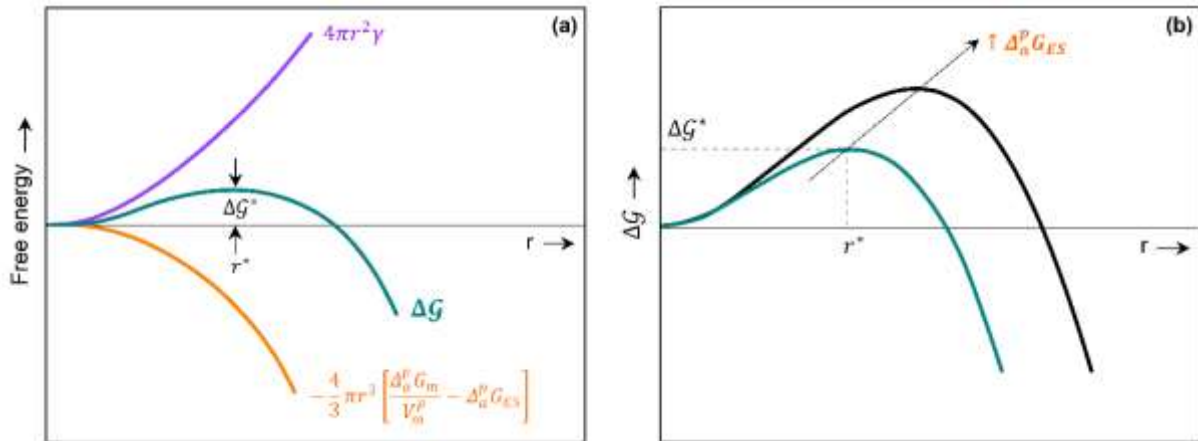


Figure 7. Schematic diagrams of (a) the component's contribution in the characteristic function ΔG (**Eq. (5)**), which gives the total free energy change between the amorphous and crystalline states, and (b) the elastic strain influence ($\Delta_a^p G_{ES}$) in ΔG (in terms of critical radius r^* and barrier to overcome ΔG^*).

It is essential to highlight the effect of temperature on the crystallization driving force during the annealing step. **Figure 8** illustrated that $\Delta_a^p G_m$ is increasingly negative when the temperature drops to the annealing temperature, inducing a smaller critical radius r^* and a barrier ΔG^* , and thus allowing the crystallization of the amorphous layer.

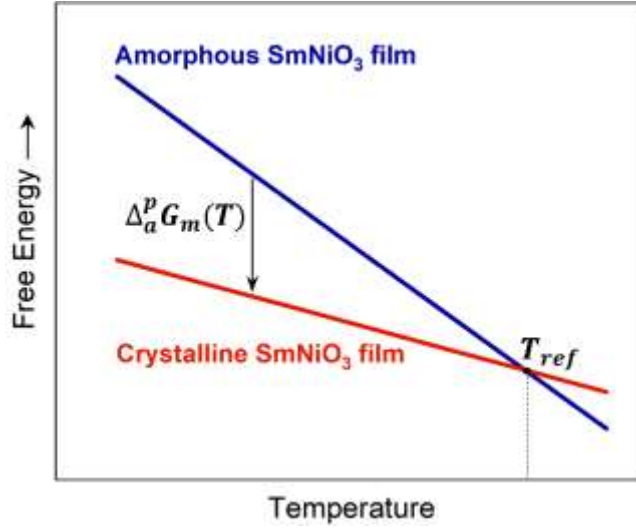


Figure 8. Schematic diagrams of the effect of temperature on the crystallization driving force ($\Delta_a^p G_m$) during the annealing step. T_{ref} is a theoretical temperature at which there is a thermodynamic equilibrium between the two phases.

On the other hand, when the perovskite phase nucleates heterogeneously at the interfaces (substrate/film and film/air surface), the characteristic function ΔG is modulated by a shape factor $S(\theta)$, allowing to define ΔG_{het} by:

$$\Delta G_{het} = \Delta G \cdot S(\theta) \quad (8)$$

where,

$$S(\theta) = \frac{1}{4} [2 + \cos \theta] [1 - \cos \theta]^2 \quad (9)$$

and, θ is the contact angle between the nucleus and the interface [70]. It is important to note that the factor $S(\theta)$ has a numerical value < 1 , which made easier to nucleate at the interfaces because the barrier height is smaller than the homogeneous nucleation one. **Figure 9(a)** displays the effect of heterogeneous nucleation on the barrier height compared to the homogeneous case. Also, for the same ΔG^* value, it has been demonstrated that a higher ΔT (difference between annealing and room temperature) is required for the spherical nuclei to be detectable, while for the same condition, the caps are already in the growth stage (**Figure 9(b)**).

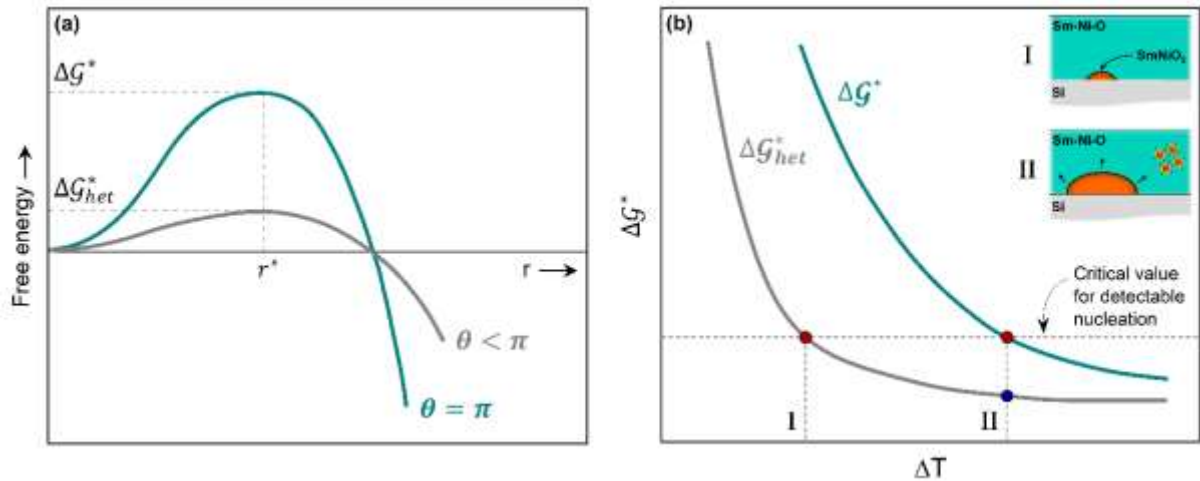


Figure 9. Comparison between homogeneous and heterogeneous nucleation. (a) Evolution of the characteristic function ΔG according to the critical radius r^* of the perovskite nuclei for homogeneous nucleation (green curve with $\theta = \pi$) and heterogeneous nucleation (grey curve with $\theta < \pi$). (b) Variation of ΔG^* with annealing (ΔT). (Note that for the same ΔG^* value, a higher ΔT is required for detectable spherical nuclei, while the caps are already in the growth stage).

Moreover, the contact angle measurement was obtained from the 5 min air-annealed sample, revealing an estimated value of θ ranging from 115° to 155° (**Figure 10**). The latter are less than 180° (π), confirming the heterogeneous nucleation in the studied SmNiO_{3- δ} thin films.

Eventually, if the ΔG^* barrier is overcome, thermodynamics indicates that perovskite nuclei can spontaneously grow since the characteristic function ΔG decreases. Nevertheless, the corresponding transformation kinetic is very small at low temperatures. Therefore, in solid phases, it is necessary to maintain the annealing temperature to ensure the growth of the nuclei, as evidenced in the preceding experimental results.

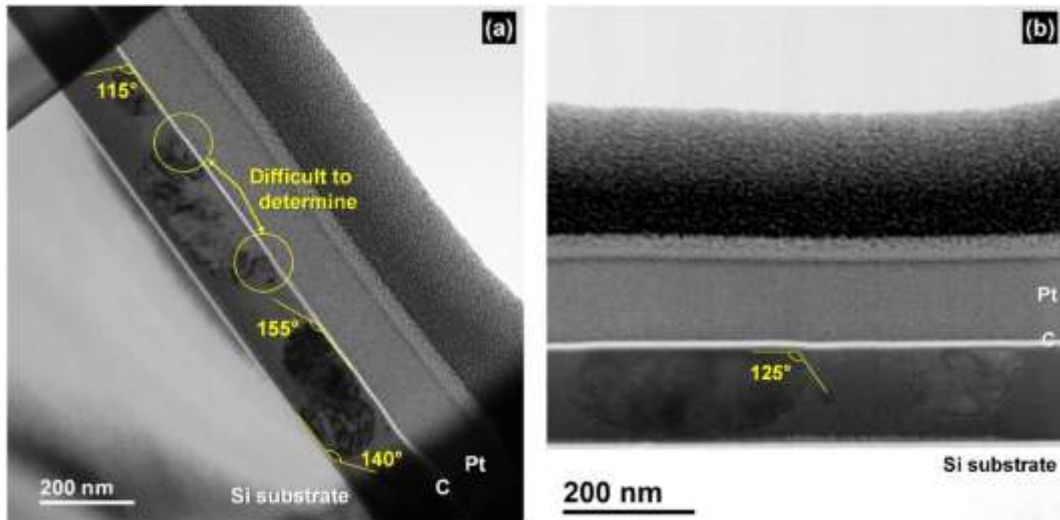


Figure 10. Contact angle (θ) measurement in two different zones for various grains of the 5 min air-annealed $\text{SmNiO}_{3-\delta}$ thin film at 500 °C.

3.4. EELS analysis of the electronic structure and valence ions progression

Another significant impact on the physical properties of nickelates is the Ni oxidation state reached by soft-annealing. Hence, the electronic structure progression with the annealing time has been investigated throughout the sample's entire thickness. To avoid the contribution of oxides at the interfaces, the analysis was performed 5 nm from them. **Figure 11(a)** assembles the broad spectra recorded by Electron Energy Loss Spectroscopy (EELS). The corresponding core excitation edge of Sm, Ni and O were identified for all the films.

Looking at each in more detail, the O *K*-edge in **Figure 11(b)** provides information about the electronic excitations from the O *1s* core level to the empty O *2p* electronic states. For rare-earth nickelates (RNiO_3), these O *2p* states are hybridized with the Ni *3d*, rare-earth *5d*, and Ni *4sp* electronic states [71]. The pre-edge peak before the threshold of oxygen *K*-edge ionization has frequently been observed in other oxides, having different interpretations [72]. However, for these perovskites, the pre-peak at 529 eV is the most analyzed because it corresponds to the Ni *3d*–O *2p* hybridization and is pretty sensitive to slight changes [73]. It has been demonstrated

how defects, faults, oxygen vacancies, and oxygen stoichiometry affected the *Ni-O* bond [28,74,75].

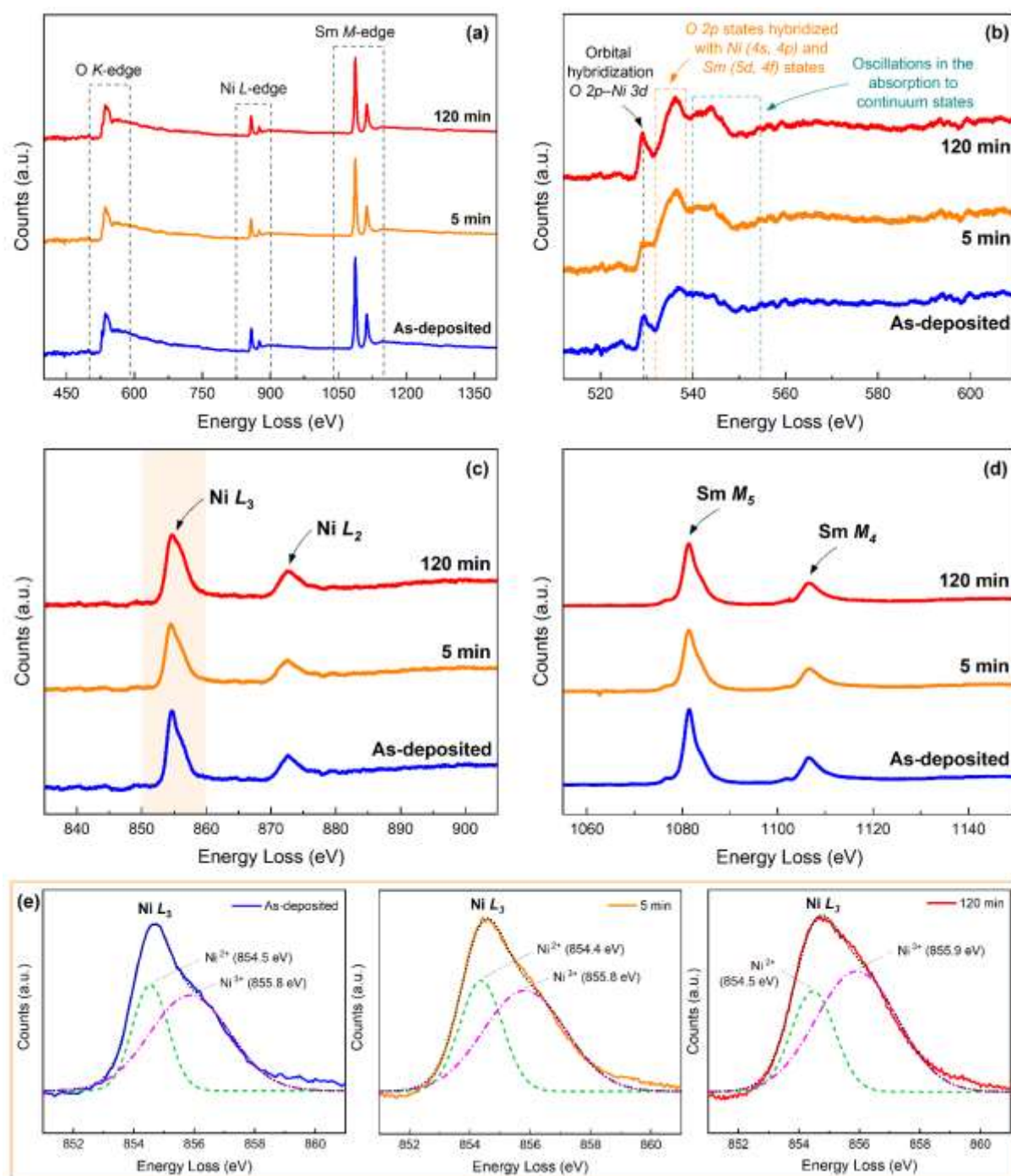


Figure 11. Electron energy loss spectroscopy (EELS) analysis of the as-deposited and air-annealed samples at 500 °C for 5 min and 120 min, respectively. (a) Broad spectrum of the core excitation edge of Sm, Ni and O elements for all the films. (b), (c) and (d) O K-edge, Ni L-edge and Sm M-edge EELS spectra. (e) Deconvolution of the Ni L₃ peak highlighted in (c) for every sample. The peaks associated with Ni²⁺ and Ni³⁺ are indicated.

Then, the pre-peak is already present for the as-deposited sample because being synthesized in a reactive atmosphere saturated with oxygen allows both Ni and Sm oxidation. However, a slight decrease in peak intensity is evident at 5 min. As a hypothesis, it can be associated with a slight loss of oxygen, defects formation, or poor crystallization with the presence of many nanocrystallites, generating measurement instabilities. Indeed, for the well-crystallized air-annealed layer for 120 min, a sharp peak is displayed, confirming the electronic structure signature in nickelates in its trivalent state. In addition, a prominent peak corresponding to the Sm $5d-O\ 2p$ hybridization emerges with annealing time. Although the latter does not generate much discussion, a discernible change due to crystallization is noticeable.

Besides that, **Figure 11(c)** depicts the Ni L -edge spectra whereby the Ni L_2 and Ni L_3 peaks depend on the Ni valence of ions. Concerning the Ni L_2 , given its shape and position, it can be assigned to the valence of Ni^{3+} . A marked difference with Ni^{2+} ion in NiO compounds (with two distinct and distant peaks) has been reported [76,77]. On the other hand, for the Ni L_3 peak it is not that immediate, even if a tiny hump is visible. Indeed, the Ni^{2+} and Ni^{3+} are normally positioned around 854.5 eV and 855.5 eV, respectively [76,78–80].

Therefore, a deconvolution of the Ni L_3 peak was carried out for the three study cases (**Figure 11(e)**). As it can be seen, the two peaks can be identified, and a continuous evolution with annealing time can be evidenced. Furthermore, with the continuous crystallization of the thin film, there is an apparent stabilization of the Ni^{3+} ion over the Ni^{2+} oxidation degree. However, the latter's contribution persists and may be associated with the presence of oxygen vacancies [75,81,82]. Lastly, for the Sm M -edge (**Figure 11(d)**), no change is evidenced, coinciding with the trivalent state of this rare-earth, which is more stable and easier to oxidize [28,83,84].

3.5. Verification of the electronic structure by XPS

Complementary to EELS, XPS analysis has been performed on as-deposited film and after annealing during 5 and 120 min. **Figure 12** presents the Sm $3d$, Ni $2p$, O $1s$ core level spectra and XPS valence band spectra of the film. It is important to note that (i) reliable literature devoted to XPS analysis on SmNiO₃ compound is limited, and (ii) no shift has been applied to the spectra to work directly on unaltered data. In addition, the shift induced by the measurement has been limited thanks to the use of a flood gun.

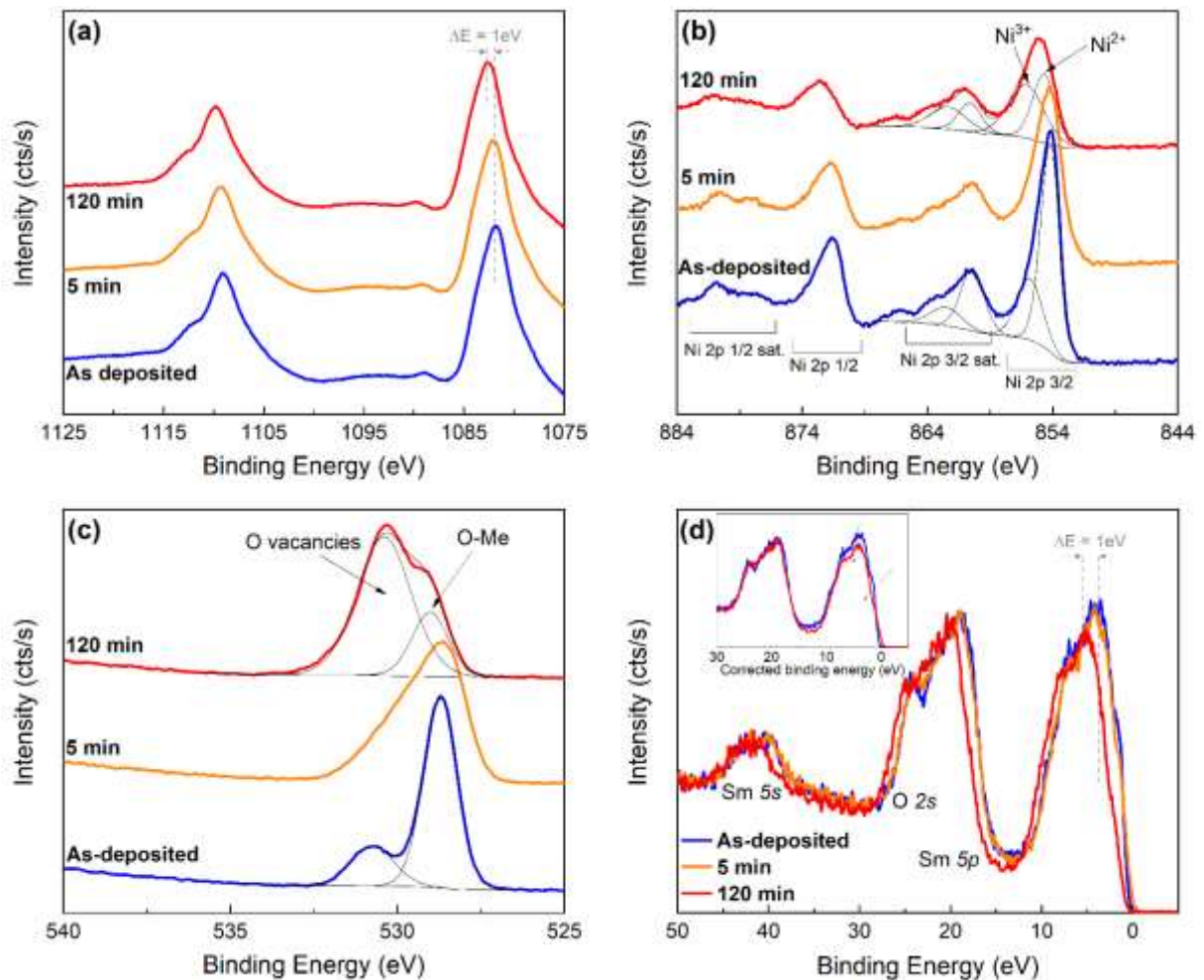


Figure 12. XPS analysis of SmNiO_{3- δ} thin films after different annealing time. (a) Sm $3d$, (b) Ni $2p$ (c) O $1s$ core level spectra and (d) XPS valence band spectra. The inset corresponds to XPS valence band, after shift of 1 eV of data after annealing for 120 min.

The Sm $3d$ signal (**Figure 12(a)**) presents a major contribution centered around 1082.7 eV (for the annealed film for 120 min), attributed to Sm^{3+} (Sm $3d$ $5/2$ contribution) and the corresponding Sm $3d$ $3/2$ contribution at 1109.7 eV. A second contribution is present as the peak shows asymmetry. A similar peak shape and position is reported for Sm^{3+} in SmNiO_3 in [85]. Such asymmetry has also been seen even for Sm^{3+} , as in Sm_2O_3 nanoparticles [86]. It is worth mentioning that Sm^{3+} is generally observed around 1083 eV [87]. As reported in [85], no significant change in the peak shape and position is noticed with annealing. Note that the shift of ≈ 1 eV for annealing of 120 min is present on all spectra (including valence band spectra), namely, it is not an intrinsic shift due to a change in the chemical environment.

The Ni $2p$ core level is more affected by the annealing step (**Figure 12(b)**). It is known that the fitting of nickel oxide signal is complex due to the multiple contributions, including plasmons and inter-band transitions, charge transfer mechanisms, and the high sensitivity to change in a chemical environment [11,88]. A single contribution per chemical state does not represent the real physical mechanism but serves as tendency determination. In this view, the Ni $2p$ $3/2$ signal is fitted with Ni^{2+} and Ni^{3+} contributions, centered at 854.7 eV and 856.1 eV, respectively (for the annealed film for 120 min). An energy difference of 1.4 eV is noticed, close to the energy difference obtained from EELS measurements ($\approx 1.4\text{eV}$) and the works from Ramanathan *et al.* ($\approx 1.5\text{eV}$), with a position at 854 and 855.5 eV for Ni^{2+} and Ni^{3+} , respectively [8,79]. The contribution at higher binding energy correspond to Ni $2p$ $3/2$ satellites peaks (858-868 eV), Ni $2p$ $1/2$ peaks (870-875 eV) and Ni $2p$ $1/2$ satellites (875-884 eV). After the annealing step, a clear change of the $\text{Ni}^{2+}/\text{Ni}^{3+}$ ratio is observed, with stabilization of Ni^{3+} , confirming the EELS results.

Interestingly, the O $1s$ signal is also largely affected by annealing (**Figure 12(c)**). Two contributions are observed at 529 and 530.4 eV. The contribution at 529 eV is attributed to metal-oxygen bound. Concerning the contribution at 530.4 eV, Kotiuga *et al.* [85] attributed it

to hydroxide contamination (and should not be included in the discussion). In contrast, other authors attributed it to oxygen vacancies [89] or also to metal oxide contribution [7]. Both explanations are acceptable, although hydroxide contamination would probably be removed after annealing. Namely, the formation of oxygen vacancies with annealing, which goes hand in hand with the decrease of the metal-oxygen bond and the change of the $\text{Ni}^{2+}/\text{Ni}^{3+}$ ratio, is more probable.

It is important to notice that Kotiuga *et al.* reported a shift in Ni 2p signal with more Ni^{2+} after low-pressure annealing of SmNiO_3 , while an opposite behavior is observed here, with stabilization of Ni^{3+} . However, in this case, the conditions are different with a potential over-stoichiometry of oxygen thanks to metastable deposition conditions and then the radiative air-annealed, which allows crystallizing $\text{SmNiO}_{3-\delta}$ compounds without high oxygen pressures.

Furthermore, **Figure 12(d)** displays the XPS valence band of the film after different annealing times. All films present contribution at 0-10 eV. At 20 eV, it is attributed to Sm 5p and O 2s orbitals, while the contribution around 42 eV is attributed to Sm 5s orbitals. With annealing, there is a slight change of level distribution, close to the Fermi level, while other contributions are not affected (see inset in **Figure 12(d)**).

3.6. Thermochromic performance through optical measurements

As Nikulin *et al.* [90] mentioned, electrical properties are affected by oxygen deficits. Therefore, to measure its impact and crystallization degree influence, FTIR measurements were conducted. Infrared optical measurement is an appealing characterization to perform since the thermochromic effect is controlled by the presence of the metal-insulator transition (MIT) phenomenon in nickelates.

The transmittance evolution of the air-annealed samples at 500 °C for 120 min and 5 min are displayed in **Figures 13(a)** and **13(b)**, respectively. As can be seen, two different behaviors under the heating ramp from 30 to 270 °C are displayed. A significant change between the first and last spectra is visible for the highly crystallized sample, while no substantial difference is observed for the 5 min sample.

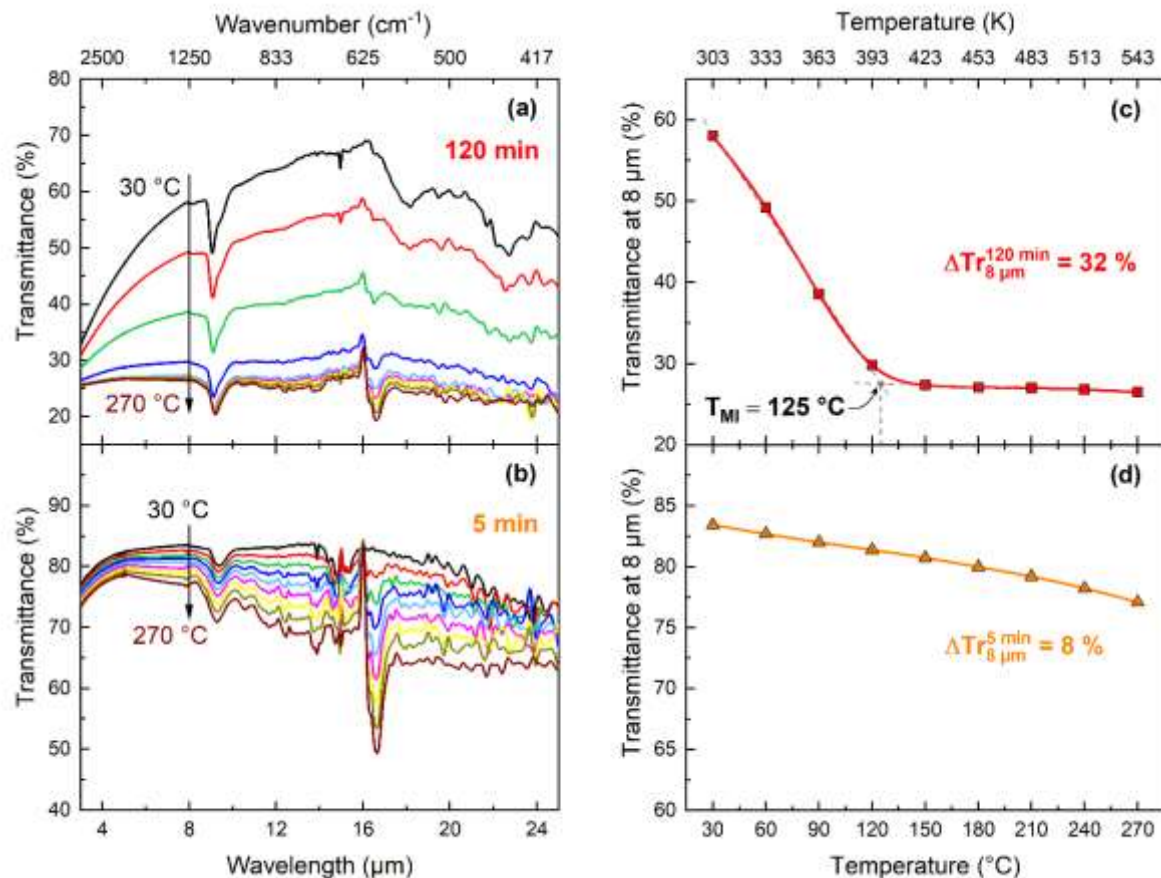


Figure 13. Optical properties of the SmNiO_{3-δ} thin film air-annealed for 5 min and 120 min at 500 °C. (a) and (b) Infrared (IR) transmittance evolution of the film in the heating ramp from 30 to 270 °C with a step of 30 °C. (c) and (d) IR transmittance performance at 8 μm *versus* temperature.

Evaluating the progression to a fixed wavelength value is practical to compare both performances. Here, it was chosen the value of 8 μm for different reasons. First, this wavelength is not influenced by the silica absorption band (around 9 μm). Also, it is situated in the atmospheric transparency band III (8-14 μm), and lastly, it is representative of thermal solar collector's infrared emissivity. Indeed, VO₂ oxides and LaCoO₃ perovskites, considered for

such application [91,92], present optical variations with the temperature at this spectrum range as a result of the thermochromic effect.

Therefore, a contrasting comparison is shown in **Figures 13(c)** and **13(d)**. For the air-annealed layer for 120 min, the transmittance decreases from 58% to 26%, and its stabilization is evident around 125 °C. It means that the $\text{SmNiO}_{3-\delta}$ thin film is thermochromic, having an optical switching of 32%, going from a more transparent state to a lesser one from low to high temperatures.

On the other hand, no optical properties can be attributed to the sample annealed for 5 min. Although a difference in transmittance of 8% was measured for the same heating range between 30 and 270 °C, it cannot be considered as a thermochromic material. A change in its behavior is expected, and probably if the temperature continues to increase, the transmittance would progressively drop without implying an optical switch at the metal-insulator transition temperature (T_{MI}). Especially in SmNiO_3 perovskites, whose T_{MI} is around 127 °C [26,93].

Hence, these results highlight the importance of obtaining a complete crystallization of SmNiO_3 thin films. With most of the layer nanocrystalline, even with some large grains, the thermochromic behavior is absent at 5 min. Likewise, even though the air-annealed sample for 120 min had a higher oxygen deficit since it was a minimal value, it did not suppress the MIT phenomenon. Conversely, such an optical switch envisages this material family as a promising candidate for solar thermal regulation.

4. CONCLUSIONS

Two significant features of *samarium nickelates* thin films have been explored in this work, providing a full understanding of the mechanisms involved in air-annealing. The first one is the study of crystallization kinetics through *in situ* HTXRD measurements. The amorphous-to-

crystalline phase transformation progression was monitored, giving access to the kinetic parameters of its evolution at different temperatures. Notably, the activation energy necessary for the $\text{SmNiO}_{3-\delta}$ nucleation was determined, whose comparison with other perovskites confirms how challenging it is to synthesize this smart material. Also, it was shown that air-annealing at very high temperatures does not favor the crystallization of these thin layers, being 500 °C, the temperature with the best compromise of time and crystallization percentage.

The second aspect concerns a thermo-kinetic approach to the crystallization mechanisms involved during air-annealing. A TEM analysis exposed the evolution of the phase transformations at different annealing times. Therefore, the correlation of the experimental results with the classical nucleation theory evidenced the combination of homogeneous and heterogeneous nucleation in the $\text{SmNiO}_{3-\delta}$ thin films throughout our synthesis process.

Furthermore, the electronic structure and the optical properties were investigated by EELS and XPS, and FTIR measurements, respectively. The stabilization progression of the Ni^{3+} oxidation degree was observed with the annealing time, in which the contribution of Ni^{2+} persisted. The latter may be associated with defects or oxygen deficits. The optical properties measurements confirmed the presence of the thermochromic effect with a transmittance change of 32%, and the metal-insulator transition temperature at 125 °C in the $\text{SmNiO}_{3-\delta}$ thin films air-annealed for 120 min. By contrast, despite having large grains, the 5 min-annealed sample did not show an optical switch because a longer annealing time is necessary to obtain excellent structural, electronic and optical properties.

In light of these outcomes, we provided the fundamental knowledge behind the soft-synthesis route described in our previous work [8]. Namely, the presented approaches allow us to understand the physical phenomena involved during $\text{SmNiO}_{3-\delta}$ thin film crystallization. From here, we overcome what has been a challenge for years in the scientific community, conferring a starting point to improve the production of nickelates and extend their uses even further.

CREDIT AUTHOR STATEMENT

Z. Fernández-Gutiérrez: Conceptualization, Investigation, Formal analysis, Writing - original draft. **S. Bruyère:** Investigation, Writing - review & editing. **D. Pilloud:** Resources, Writing - review & editing. **E. Hays:** Investigation, Writing - review & editing. **G. Medjahdi:** Investigation. **S. Barrat:** Conceptualization, Writing - review & editing, Supervision. **F. Capon:** Writing - review & editing, Supervision, Funding acquisition.

DECLARATION OF COMPETING INTEREST

The authors declare that they have no known competing financial interests or personal relationships that could have appeared to influence the work reported in this paper.

ACKNOWLEDGMENTS

This work was supported partly by the French PIA project “Lorraine Université d’Excellence”, reference ANR-15-IDEX-04-LUE. The authors acknowledge Pascal Boulet and the XGamma Competence Center (CC-X γ) of the Institut Jean Lamour (IJL) for the diffractometers provision and their technical support.

REFERENCES

- [1] Z. Li, Y. Zhou, H. Qi, Q. Pan, Z. Zhang, N.N. Shi, M. Lu, A. Stein, C.Y. Li, S. Ramanathan, N. Yu, Correlated Perovskites as a New Platform for Super-Broadband-Tunable Photonics, *Adv. Mater.* 28 (2016) 9117–9125. <https://doi.org/https://doi.org/10.1002/adma.201601204>.
- [2] J. Rensberg, S. Zhang, Y. Zhou, A.S. McLeod, C. Schwarz, M. Goldflam, M. Liu, J. Kerbusch, R. Nawrodt, S. Ramanathan, D.N. Basov, F. Capasso, C. Ronning, M.A. Kats, Active Optical Metasurfaces Based on Defect-Engineered Phase-Transition Materials, *Nano Lett.* 16 (2016). <https://doi.org/10.1021/acs.nanolett.5b04122>.
- [3] F. Capon, D. Horwat, J.F. Pierson, M. Zaghrioui, P. Laffez, Thermo-chromic effect in NdNiO₃- δ thin films annealed in ambient air, *J. Phys. D. Appl. Phys.* 42 (2009). <https://doi.org/10.1088/0022-3727/42/18/182006>.
- [4] A. Boileau, F. Capon, P. Laffez, S. Barrat, J.L. Endrino, R. Escobar Galindo, D. Horwat, J.F. Pierson, Mechanisms of oxidation of NdNiO₃- δ thermo-chromic thin films synthesized by a two-step method in soft conditions, *J. Phys. Chem. C.* 118 (2014) 5908–5917.

- <https://doi.org/10.1021/jp4111597>.
- [5] L. Chang, L. Wang, L. You, Y. Zhou, L. Fang, S. Wang, J. Wang, Band gap tuning of nickelates for photovoltaic applications, *J. Phys. D. Appl. Phys.* 49 (2016). <https://doi.org/10.1088/0022-3727/49/44/44LT02>.
 - [6] L. Wang, S. Dash, L. Chang, L. You, Y. Feng, X. He, K.J. Jin, Y. Zhou, H.G. Ong, P. Ren, S. Wang, L. Chen, J. Wang, Oxygen Vacancy Induced Room-Temperature Metal-Insulator Transition in Nickelate Films and Its Potential Application in Photovoltaics, *ACS Appl. Mater. Interfaces.* 8 (2016) 9769–9776. <https://doi.org/10.1021/acsami.6b00650>.
 - [7] H. Bao, M. Du, H. Wang, K. Wang, X. Zuo, F. Liu, L. Liu, D. Eder, A. Cherevan, S. Wang, L. Wan, S. Zhao, S. Liu, Samarium-Doped Nickel Oxide for Superior Inverted Perovskite Solar Cells: Insight into Doping Effect for Electronic Applications, *Adv. Funct. Mater.* 31 (2021) 1–9. <https://doi.org/10.1002/adfm.202102452>.
 - [8] S.D. Ha, G.H. Aydogdu, S. Ramanathan, Metal-insulator transition and electrically driven memristive characteristics of SmNiO₃ thin films, *Appl. Phys. Lett.* 98 (2011). <https://doi.org/10.1063/1.3536486>.
 - [9] C. Oh, S. Heo, H.M. Jang, J. Son, Correlated memory resistor in epitaxial NdNiO₃ heterostructures with asymmetrical proton concentration, *Appl. Phys. Lett.* 108 (2016). <https://doi.org/10.1063/1.4944842>.
 - [10] S.D. Ha, J. Shi, Y. Meroz, L. Mahadevan, S. Ramanathan, Neuromimetic circuits with synaptic devices based on strongly correlated electron systems, *Phys. Rev. Appl.* 2 (2014). <https://doi.org/10.1103/PhysRevApplied.2.064003>.
 - [11] J. Shi, Y. Zhou, S. Ramanathan, Colossal resistance switching and band gap modulation in a perovskite nickelate by electron doping, *Nat. Commun.* 5 (2014) 1–9. <https://doi.org/10.1038/ncomms5860>.
 - [12] J. Son, S. Rajan, S. Stemmer, S. James Allen, A heterojunction modulation-doped Mott transistor, *J. Appl. Phys.* 110 (2011). <https://doi.org/10.1063/1.3651612>.
 - [13] J. Shi, S.D. Ha, Y. Zhou, F. Schoofs, S. Ramanathan, A correlated nickelate synaptic transistor, *Nat. Commun.* 4 (2013). <https://doi.org/10.1038/ncomms3676>.
 - [14] Z. Li, F. Yan, X. Li, Y. Cui, V. Wang, J. Wang, C. Liu, Y. Jiang, N. Chen, J. Chen, Molten-salt synthesis of rare-earth nickelate electronic transition semiconductors at medium high metastability, *Scr. Mater.* 207 (2022) 114271. <https://doi.org/10.1016/j.scriptamat.2021.114271>.
 - [15] H. LaBollita, A.S. Botana, Electronic structure and magnetic properties of higher-order layered nickelates, *Phys. Rev. B.* 104 (2021). <https://doi.org/10.1103/PhysRevB.104.035148>.
 - [16] C.J. Anjeline, B.G. Marate, D. Velu, S.M.S. Kumar, N. Lakshminarasimhan, Probing oxygen vacancy-induced mixed-valence states of nickel in LaNiO₃ and their influence on electrocatalytic and magnetic properties, *Mater. Chem. Phys.* 288 (2022). <https://doi.org/10.1016/j.matchemphys.2022.126331>.
 - [17] K. Ramadoss, N. Mandal, X. Dai, Z. Wan, Y. Zhou, L. Rokhinson, Y.P. Chen, J. Hu, S. Ramanathan, Sign reversal of magnetoresistance in a perovskite nickelate by electron doping, *Phys. Rev. B.* (2016). <https://doi.org/10.1103/PhysRevB.94.235124>.
 - [18] J. Van Den Brink, D.I. Khomskii, Multiferroicity due to charge ordering, *J. Phys. Condens. Matter.* 20 (2008). <https://doi.org/10.1088/0953-8984/20/43/434217>.
 - [19] S.W. Cheong, M. Mostovoy, Multiferroics: A magnetic twist for ferroelectricity, *Nat. Mater.* 6 (2007). <https://doi.org/10.1038/nmat1804>.
 - [20] G. Catalan, Progress in perovskite nickelate research, *Phase Transitions.* 81 (2008) 729–749. <https://doi.org/10.1080/01411590801992463>.
 - [21] D.K. Hwang, S. Kim, J.H. Lee, I.S. Hwang, I.D. Kim, Phase evolution of perovskite LaNiO₃ nanofibers for supercapacitor application and p-type gas sensing properties of LaOCl-NiO composite nanofibers, *J. Mater. Chem.* 21 (2011). <https://doi.org/10.1039/c0jm02256j>.
 - [22] L. Hu, Y. Deng, K. Liang, X. Liu, W. Hu, LaNiO₃/NiO hollow nanofibers with mesoporous wall: a significant improvement in NiO electrodes for supercapacitors, *J. Solid State Electrochem.* 19 (2015). <https://doi.org/10.1007/s10008-014-2641-6>.

- [23] Y. Cao, B. Lin, Y. Sun, H. Yang, X. Zhang, Sr-doped lanthanum nickelate nanofibers for high energy density supercapacitors, *Electrochim. Acta.* 174 (2015). <https://doi.org/10.1016/j.electacta.2015.05.131>.
- [24] T.R. Ling, Z.B. Chen, M.D. Lee, Studies on catalytic and conductive properties of LaNiO₃ for oxidation of C₂H₅OH, H₂CO, and CH₄, *Catal. Today.* 26 (1995). [https://doi.org/10.1016/0920-5861\(95\)00099-2](https://doi.org/10.1016/0920-5861(95)00099-2).
- [25] L. Xuchen, X. Tingxian, D. Xianghong, Preparation and characterization of LaNiO₃ A/F ratio-sensitive thin film by sol-gel process based on amorphous citrate precursors, *Sensors Actuators, B Chem.* 67 (2000). [https://doi.org/10.1016/S0925-4005\(99\)00379-2](https://doi.org/10.1016/S0925-4005(99)00379-2).
- [26] P. Lacorre, J.B. Torrance, J. Pannetier, A.I. Nazzal, P.W. Wang, T.C. Huang, Synthesis, Crystal Structure, and Properties of Metallic PrNiO₃: Comparison with Metallic NdNiO₃ and Semiconducting SmNiO₃, *J. Solid State Chem.* 91 (1991) 225–237. [https://doi.org/10.1016/0022-4596\(91\)90077-U](https://doi.org/10.1016/0022-4596(91)90077-U).
- [27] L. Medarde, Structural, magnetic and electronic properties of RNiO₃ perovskites (R = rare earth), *J. Phys. Condens. Matter.* 9 (1997) 1679–1707. <http://iopscience.iop.org/0953-8984/9/8/003>.
- [28] Q. Zhong, X. Deng, L. Lin, H. Song, Y. Zheng, Y. Cheng, P. Xiang, N. Zhong, R. Qi, C. Duan, R. Huang, Revealing a high-density three-dimensional Ruddlesden–Popper-type fault network in an SmNiO₃ thin film, *J. Mater. Res.* 36 (2021) 1637–1645. <https://doi.org/10.1557/s43578-021-00145-1>.
- [29] T. Mizokawa, A. Fujimori, H. Namatame, K. Akeyama, N. Kosugi, Electronic structure of the local-singlet insulator NaCuO₂, *Phys. Rev. B.* 49 (1994) 7193. <https://doi.org/10.1103/PhysRevB.49.7193>.
- [30] M. Imada, A. Fujimori, T. Yoshinori, Metal-insulator transition, *Rev. Mod. Phys.* 70 (1998) 1039. <https://doi.org/10.1103/RevModPhys.70.1039>.
- [31] J.B. Torrance, P. Lacorre, A.I. Nazzal, E.J. Ansaldo, C. Niedermayer, Systematic study of insulator-metal transitions in perovskites RNiO₃ (R=Pr,Nd,Sm,Eu) due to closing of charge-transfer gap, *Phys. Rev. B.* 45 (1992) 8209–8212. <https://doi.org/10.1103/PhysRevB.45.8209>.
- [32] F. Capon, P. Ruello, J.F. Bardeau, P. Simon, P. Laffez, B. Dkhil, L. Reversat, K. Galicka, A. Ratuszna, Metal-insulator transition in thin films of RxR'1-xNiO₃ compounds: DC electrical conductivity and IR spectroscopy measurements, *J. Phys. Condens. Matter.* 17 (2005) 1137–1150. <https://doi.org/10.1088/0953-8984/17/7/007>.
- [33] S. Catalano, M. Gibert, J. Fowlie, J. Iñiguez, J.M. Triscone, J. Kreisel, Rare-earth nickelates RNiO₃: Thin films and heterostructures, *Reports Prog. Phys.* 81 (2018). <https://doi.org/10.1088/1361-6633/aaa37a>.
- [34] G. Demazeau, A. Marbeuf, M. Pouchard, Sur une série de composés oxygènes du nickel trivalent dérivés de la perovskite, *J. Solid State Chem.* 3 (1971) 582–589. [https://doi.org/10.1016/0022-4596\(71\)90105-8](https://doi.org/10.1016/0022-4596(71)90105-8).
- [35] R. Jaramillo, F. Schoofs, S.D. Ha, S. Ramanathan, High pressure synthesis of SmNiO₃ thin films and implications for thermodynamics of the nickelates, *J. Mater. Chem. C.* 1 (2013) 2455–2462. <https://doi.org/10.1039/c3tc00844d>.
- [36] F. Capon, P. Laffez, J.F. Bardeau, P. Simon, P. Lacorre, M. Zaghrioui, Metal-insulator transition at room temperature and infrared properties of Nd_{0.7}Eu_{0.3}NiO₃ thin films, *Appl. Phys. Lett.* 81 (2002) 619–621. <https://doi.org/10.1063/1.1493645>.
- [37] P. Laffez, M. Zaghrioui, I. Monot, T. Brousse, P. Lacorre, Microstructure and metal-insulator transition of NdNiO₃ thin films on various substrates, *Thin Solid Films.* 354 (1999) 50–54. [https://doi.org/10.1016/S0040-6090\(99\)00557-X](https://doi.org/10.1016/S0040-6090(99)00557-X).
- [38] C. Napierala, C. Lepoittevin, M. Edely, L. Sauques, F. Giovanelli, P. Laffez, G. VanTedeloo, Moderate pressure synthesis of rare earth nickelate with metal-insulator transition using polymeric precursors, *J. Solid State Chem.* 183 (2010) 1663–1669. <https://doi.org/10.1016/j.jssc.2010.04.019>.
- [39] F. Yan, Z. Mi, J. Chen, H. Hu, L. Gao, J. Wang, N. Chen, Y. Jiang, L. Qiao, J. Chen, Revealing

- the role of interfacial heterogeneous nucleation in the metastable thin film growth of rare-earth nickelate electronic transition materials, *Phys. Chem. Chem. Phys.* 24 (2022) 9333–9344. <https://doi.org/10.1039/d1cp05347g>.
- [40] B. Viswanath, G.H. Aydogdu, S.D. Ha, S. Ramanathan, In situ stress relaxation and diffraction studies across the metal-insulator transition in epitaxial and polycrystalline SmNiO₃ thin films, *Scr. Mater.* 66 (2012) 463–466. <https://doi.org/10.1016/j.scriptamat.2011.12.018>.
- [41] Q. Guo, S. Farokhipoor, C. Magén, F. Rivadulla, B. Noheda, Tunable resistivity exponents in the metallic phase of epitaxial nickelates, *Nat. Commun.* 11 (2020) 1–9. <https://doi.org/10.1038/s41467-020-16740-5>.
- [42] T. Shao, Z. Qi, Y. Wang, Y. Li, M. Yang, C. Hu, Metal-insulator transition in epitaxial NdNiO₃ thin film: A structural, electrical and optical study, *Appl. Surf. Sci.* 399 (2017) 346–350. <https://doi.org/10.1016/j.apsusc.2016.12.102>.
- [43] C. Domínguez, A.B. Georgescu, B. Mundet, Y. Zhang, J. Fowlie, A. Mercy, A. Waelchli, S. Catalano, D.T.L. Alexander, P. Ghosez, A. Georges, A.J. Millis, M. Gibert, J.M. Triscone, Length scales of interfacial coupling between metal and insulator phases in oxides, *Nat. Mater.* 19 (2020) 1182–1187. <https://doi.org/10.1038/s41563-020-0757-x>.
- [44] B. Torriss, J. Margot, M. Chaker, Metal-insulator transition of strained SmNiO₃ thin films: Structural, electrical and optical properties, *Sci. Rep.* 7 (2017) 1–9. <https://doi.org/10.1038/srep40915>.
- [45] S. Middey, J. Chakhalian, P. Mahadevan, J.W. Freeland, A.J. Millis, D.D. Sarma, Physics of Ultrathin Films and Heterostructures of Rare-Earth Nickelates, *Annu. Rev. Mater. Res.* 46 (2016) 305–334. <https://doi.org/10.1146/annurev-matsci-070115-032057>.
- [46] J. Chen, A. Bird, F. Yan, W. Wu, X. Ke, Y. Jiang, N. Chen, Mechanical and correlated electronic transport properties of preferentially orientated SmNiO₃ films, *Ceram. Int.* 46 (2020) 6693–6697. <https://doi.org/10.1016/j.ceramint.2019.11.157>.
- [47] F. Conchon, A. Boule, R. Guinebretière, E. Dooryhée, J.L. Hodeau, C. Girardot, S. Pignard, J. Kreisel, F. Weiss, The role of strain-induced structural changes in the metal-insulator transition in epitaxial SmNiO₃ films, *J. Phys. Condens. Matter.* 20 (2008) 145216. <https://doi.org/10.1088/0953-8984/20/14/145216>.
- [48] Z. Fernández-Gutiérrez, D. Pilloud, S. Bruyère, A. Didelot, D.N. Kharkhan, S. Barrat, F. Capon, Thermochromic SmNiO₃- δ thin films deposited by magnetron sputtering and crystallized by soft-annealing in air, *Scr. Mater.* 218 (2022) 114795. <https://doi.org/10.1016/j.scriptamat.2022.114795>.
- [49] P. Laffez, M. Zaghrioui, R. Retoux, P. Lacorre, Oriented and polycrystalline NdNiO₃ thin films on silicon substrate, *J. Magn. Magn. Mater.* 211 (2000) 111–117. [https://doi.org/10.1016/S0304-8853\(99\)00721-0](https://doi.org/10.1016/S0304-8853(99)00721-0).
- [50] R.W. Schwartz, J.A. Voigt, B.A. Tuttle, D.A. Payne, T.L. Reichert, R.S. DaSalla, Comments on the effects of solution precursor characteristics and thermal processing conditions on the crystallization behavior of sol-gel derived lead zirconate titanate thin films, *J. Mater. Res.* 12 (1997) 444–456. <https://doi.org/10.1557/JMR.1997.0066>.
- [51] R. Scherwitzl, P. Zubko, C. Lichtensteiger, J.M. Triscone, Electric-field tuning of the metal-insulator transition in ultrathin films of LaNiO₃, *Appl. Phys. Lett.* 95 (2009). <https://doi.org/10.1063/1.3269591>.
- [52] V.I. Kalikmanov, Classical Nucleation Theory. In: *Nucleation Theory. Lecture Notes in Physics*, Springer, Dordrecht, 2013. https://doi.org/10.1007/978-90-481-3643-8_3.
- [53] A.N. Kolmogorov, On the statistical theory of the crystallization of metals, *Bull. Acad. Sci. USSR, Math. Ser.* 1 (1937).
- [54] M. Avrami, Kinetics of phase change. I: General theory, *J. Chem. Phys.* 7 (1939) 1103–1112. <https://doi.org/10.1063/1.1750380>.
- [55] W.A. Johnson, R.F. Mehl, Reaction Kinetics in Processes of Nucleation and Growth, *Trans. Am. Inst. Minning Metall. Eng.* 135 (1939).
- [56] M. Avrami, Kinetics of Phase Change. II Transformation-Time Relations for Random

- Distribution of Nuclei, *J. Chem. Phys.* 8 (1940) 212. <https://doi.org/10.1063/1.1750631>.
- [57] M. Avrami, Granulation, phase change, and microstructure kinetics of phase change. III, *J. Chem. Phys.* 9 (1941) 177–184. <https://doi.org/10.1063/1.1750872>.
- [58] M.M. Moghadam, P.W. Voorhees, Thin film phase transformation kinetics: From theory to experiment, *Scr. Mater.* 124 (2016) 164–168. <https://doi.org/10.1016/j.scriptamat.2016.07.010>.
- [59] E.L. Pang, N.Q. Vo, T. Philippe, P.W. Voorhees, Modeling interface-controlled phase transformation kinetics in thin films, *J. Appl. Phys.* 117 (2015) 1–8. <https://doi.org/10.1063/1.4919725>.
- [60] K.N.P. Kumar, K. Keizer, A.J. Burggraaf, Textural evolution and phase transformation in titania membranes: Part 1.—unsupported membranes, *J. Mater. Chem.* 3 (1993) 1141–1149. <https://doi.org/10.1039/JM9930301141>.
- [61] L. Zhang, X. Luo, J.D. Zhang, Y.F. Long, X. Xue, B.J. Xu, Kinetic Study on the Crystal Transformation of Fe-Doped TiO₂ via in Situ High-Temperature X-ray Diffraction and Transmission Electron Microscopy, *ACS Omega*. 6 (2021) 965–975. <https://doi.org/10.1021/acsomega.0c05609>.
- [62] M.G. Kang, M.S. Noh, J.J. Pyeon, W.S. Jung, H.G. Moon, S.H. Baek, S. Nahm, S.J. Yoon, C.Y. Kang, Direct Growth of Ferroelectric Oxide Thin Films on Polymers through Laser-Induced Low-Temperature Liquid-Phase Crystallization, *Chem. Mater.* 32 (2020) 6483–6493. <https://doi.org/10.1021/acs.chemmater.0c01742>.
- [63] E. Haye, F. Capon, S. Barrat, P. Boulet, E. Andre, C. Carteret, S. Bruyere, Properties of rare-earth orthoferrites perovskite driven by steric hindrance, *J. Alloys Compd.* 657 (2016) 631–638. <https://doi.org/10.1016/j.jallcom.2015.10.135>.
- [64] Z. Zhu, Y. Long, X. Xue, Y. Yin, B. Zhu, B. Xu, Phase-transition kinetics of calcium-doped TiO₂: A high-temperature XRD study, *Ceram. Int.* (2022). <https://doi.org/10.1016/j.ceramint.2022.05.160>.
- [65] F. Conchon, A. Boulle, R. Guinebretière, E. Dooryhée, J.L. Hodeau, C. Girardot, S. Pignard, J. Kreisel, F. Weiss, L. Libralesso, T.L. Lee, Investigation of strain relaxation mechanisms and transport properties in epitaxial SmNiO₃ films, *J. Appl. Phys.* 103 (2008). <https://doi.org/10.1063/1.2938845>.
- [66] P. Stadelmann, JEMS Java Electron microscopy software, (2020). <https://www.jems-swiss.ch/>.
- [67] M. Ohring, *Materials Science of Thin Films*, 2013. <https://doi.org/10.1016/C2009-0-22199-4>.
- [68] I. Bretos, R. Jiménez, J. Ricote, M.L. Calzada, Low-temperature crystallization of solution-derived metal oxide thin films assisted by chemical processes, *Chem. Soc. Rev.* 47 (2018) 291–308. <https://doi.org/10.1039/c6cs00917d>.
- [69] V. Raghavan, M. Cohen, *Solid-State Phase Transformations*, in: N.B. Hannay (Ed.), Chang. State, Springer US, Boston, MA, 1975: pp. 67–127. https://doi.org/10.1007/978-1-4757-1120-2_2.
- [70] S. Song, M.T. Hörantner, K. Choi, H.J. Snaith, T. Park, Inducing swift nucleation morphology control for efficient planar perovskite solar cells by hot-air quenching, *J. Mater. Chem. A*. 5 (2017) 3812–3818. <https://doi.org/10.1039/c6ta09020f>.
- [71] B. Mundet, C. Domínguez, J. Fowlie, M. Gibert, J.M. Triscone, D.T.L. Alexander, Near-Atomic-Scale Mapping of Electronic Phases in Rare Earth Nickelate Superlattices, *Nano Lett.* 21 (2021) 2436–2443. <https://doi.org/10.1021/acs.nanolett.0c04538>.
- [72] S. Lafuerza, G. Subías, J. García, S. Di Matteo, J. Blasco, V. Cuartero, C.R. Natoli, Origin of the pre-peak features in the oxygen K-edge x-ray absorption spectra of LaFeO₃ and LaMnO₃ studied by Ga substitution of the transition metal ion, *J. Phys. Condens. Matter*. 23 (2011) 325601. <https://doi.org/10.1088/0953-8984/23/32/325601>.
- [73] M.N. Grisolia, J. Varignon, G. Sanchez-Santolino, A. Arora, S. Valencia, M. Varela, R. Abrudan, E. Weschke, E. Schierle, J.E. Rault, J.-P. Rueff, A. Barthélémy, J. Santamaria, M. Bibes, Hybridization-controlled charge transfer and induced magnetism at correlated oxide interfaces, *Nat. Phys.* 12 (2016) 484–492. <https://doi.org/10.1038/nphys3627>.
- [74] M. Abbate, G. Zampieri, F. Prado, A. Caneiro, J.M. Gonzalez-Calbet, M. Vallet-Regi, Electronic structure and metal-insulator transition in LaNiO_{3-d}, *Phys. Rev. B*. 65 (2002) 155101.

- <https://doi.org/10.1103/PhysRevB.65.155101>.
- [75] L. Wang, Q. Zhang, L. Chang, L. You, X. He, K. Jin, L. Gu, H. Guo, C. Ge, Y. Feng, J. Wang, Electrochemically Driven Giant Resistive Switching in Perovskite Nickelates Heterostructures, *Adv. Electron. Mater.* 3 (2017) 1–7. <https://doi.org/10.1002/aelm.201700321>.
- [76] M. Medarde, A. Fontaine, J. García-Muñoz, J. Rodríguez-Carvajal, M. de Santis, M. Sacchi, G. Rossi, P. Lacorre, RNiO₃ perovskites (R=Pr,Nd): Nickel valence and the metal-insulator transition investigated by x-ray-absorption spectroscopy, *Phys. Rev. B.* 46 (1992) 14975–14984. <https://doi.org/10.1103/physrevb.46.14975>.
- [77] T.H. Kim, T.R. Paudel, R.J. Green, K. Song, H.S. Lee, S.Y. Choi, J. Irwin, B. Noesges, L.J. Brillson, M.S. Rzchowski, G.A. Sawatzky, E.Y. Tsymbal, C.B. Eom, Strain-driven disproportionation at a correlated oxide metal-insulator transition, *Phys. Rev. B.* 101 (2020) 1–7. <https://doi.org/10.1103/PhysRevB.101.121105>.
- [78] G. Tyuliev, M. Sokolova, Temperature dependence of Ni³⁺ quantity in the surface layer of NiO, *Appl. Surf. Sci.* 52 (1991) 343–349. [https://doi.org/10.1016/0169-4332\(91\)90078-X](https://doi.org/10.1016/0169-4332(91)90078-X).
- [79] G.H. Aydogdu, S.D. Ha, B. Viswanath, S. Ramanathan, Epitaxy, strain, and composition effects on metal-insulator transition characteristics of SmNiO₃ thin films, *J. Appl. Phys.* 109 (2011) 124110. <https://doi.org/10.1063/1.3598055>.
- [80] A. Boileau, F. Capon, R. Coustel, P. Laffez, S. Barrat, J.F. Pierson, Inductive effect of nd for Ni³⁺ stabilization in NdNiO₃ Synthesized by Reactive DC Cosputtering, *J. Phys. Chem. C.* 121 (2017) 21579–21590. <https://doi.org/10.1021/acs.jpcc.7b02251>.
- [81] J.W. Freeland, M. Van Veenendaal, J. Chakhalian, Evolution of electronic structure across the rare-earth RNiO₃ series, *J. Electron Spectros. Relat. Phenomena.* 208 (2016) 56–62. <https://doi.org/10.1016/j.elspec.2015.07.006>.
- [82] J. Wang, L. Wang, L. Chang, X. Yin, L. You, J.L. Zhao, H. Guo, K. Jin, K. Ibrahim, J. Wang, A. Rusydi, Self-powered sensitive and stable UV-visible photodetector based on GdNiO₃/Nb-doped SrTiO₃ heterojunctions, *Appl. Phys. Lett.* 110 (2017) 1–5. <https://doi.org/10.1063/1.4974144>.
- [83] G. Kaindl, G. Kalkowski, W.D. Brewer, B. Perscheid, F. Holtzberg, M-edge x-ray absorption spectroscopy of 4f instabilities in rare-earth systems (invited), *J. Appl. Phys.* 55 (1984) 1910–1915. <https://doi.org/10.1063/1.333517>.
- [84] T. Okazaki, K. Suenaga, Y. Lian, Z. Gu, H. Shinohara, Direct EELS observation of the oxidation states of Sm atoms in Sm@C_{2n} metallofullerenes (74 ≤ 2n ≤ 84), *J. Chem. Phys.* 113 (2000) 9593–9597. <https://doi.org/10.1063/1.1321047>.
- [85] M. Kotiuga, Z. Zhang, J. Li, F. Rodolakis, H. Zhou, R. Sutarto, F. He, Q. Wang, Y. Sun, Y. Wang, N.A. Aghamiri, S.B. Hancock, L.P. Rokhinson, D.P. Landau, Y. Abate, J.W. Freeland, R. Comin, S. Ramanathan, K.M. Rabe, Carrier localization in perovskite nickelates from oxygen vacancies, *Proc. Natl. Acad. Sci.* 116 (2019) 21992–21997. <https://doi.org/10.1073/pnas.1910490116>.
- [86] B.T. Sone, E. Manikandan, A. Gurib-Fakim, M. Maaza, Sm₂O₃ nanoparticles green synthesis via *Callistemon viminalis*’ extract, *J. Alloys Compd.* 650 (2015) 357–362. <https://doi.org/10.1016/j.jallcom.2015.07.272>.
- [87] K. Myhre, J. Burns, H. Meyer, N. Sims, R. Boll, Samarium electrodeposited acetate and oxide thin films on stainless steel substrate characterized by XPS, *Surf. Sci. Spectra.* 23 (2016) 70–81. <https://doi.org/10.1116/1.4954390>.
- [88] A.P. Grosvenor, M.C. Biesinger, R.S.C. Smart, N.S. McIntyre, New interpretations of XPS spectra of nickel metal and oxides, 600 (2006) 1771–1779. <https://doi.org/10.1016/j.susc.2006.01.041>.
- [89] D.H. Yoon, Y.J. Tak, S.P. Park, J. Jung, H. Lee, H.J. Kim, Simultaneous engineering of the interface and bulk layer of Al/sol-NiO x/Si structured resistive random access memory devices, *J. Mater. Chem. C.* 2 (2014) 6148–6154. <https://doi.org/10.1039/c4tc00858h>.
- [90] I. V. Nikulin, M.A. Novojilov, A.R. Kaul, S.N. Mudretsova, S. V. Kondrashov, Oxygen nonstoichiometry of NdNiO_{3-δ} and SmNiO_{3-δ}, *Mater. Res. Bull.* 39 (2004) 775–791.

<https://doi.org/10.1016/j.materresbull.2004.02.005>.

- [91] D. Mercs, A. Didelot, F. Capon, J.F. Pierson, B. Hafner, A. Pazidis, S. Föste, R. Reineke-Koch, Innovative Smart Selective Coating to Avoid Overheating in Highly Efficient Thermal Solar Collectors, *Energy Procedia*. 91 (2016) 84–93. <https://doi.org/10.1016/j.egypro.2016.06.177>.
- [92] D.N. Kharkhan, A. Didelot, D. Pilloud, S. Bruyère, D. Mangin, S. Migot, S. Barrat, Z. Fernández-Gutiérrez, N. Portha, F. Capon, Thermochromic LaCoO₃ selective layer for self-regulated thermal solar collectors, *Sol. Energy Mater. Sol. Cells*. 240 (2022) 1–9. <https://doi.org/10.1016/j.solmat.2022.111690>.
- [93] M. Medarde, C. Dallera, M. Grioni, B. Delley, F. Vernay, J. Mesot, M. Sikora, J.A. Alonso, M.J. Martínez-Lope, Charge disproportionation in R NiO₃ perovskites (R=rare earth) from high-resolution x-ray absorption spectroscopy, *Phys. Rev. B - Condens. Matter Mater. Phys.* 80 (2009) 9–11. <https://doi.org/10.1103/PhysRevB.80.245105>.